TUNING THE HYDROGEN EVOLUTION ACTIVITY OF BETA PHASE MO_2C NANOPARTICLES VIA CONTROL OF THEIR GROWTH CONDITIONS

by

Timothy T. Yang

B. S. in Physics, University of California, Santa Barbara, 2013

Submitted to the Graduate Faculty of

Swanson School of Engineering in partial fulfillment

of the requirements for the degree of

Master of Science

University of Pittsburgh

2017

UNIVERSITY OF PITTSBURGH

SWANSON SCHOOL OF ENGINEERING

This thesis was presented

by

Timothy T. Yang

It was defended on

April 3, 2017

and approved by

Jung-Kun Lee, PhD, Associate Professor
Department of Mechanical Engineering and Materials Science

Guofeng Wang, PhD, Associate Professor
Department of Mechanical Engineering and Materials Science

Thesis Advisor: Wissam Saidi, PhD, Associate Professor
Department of Mechanical Engineering and Materials Science

TUNING THE HYDROGEN EVOLUTION ACTIVITY OF BETA PHASE MO_2C NANOPARTICLES VIA CONTROL OF THEIR GROWTH CONDITIONS

Timothy T. Yang, M.S.

University of Pittsburgh, 2017

The use of water electrocatalysis for hydrogen production is a promising, sustainable, and greenhouse-gas-free process to develop disruptive renewable energy technologies. Transition metal carbides, the β-phase Mo_2C, are garnering increased attention as hydrogen evolution reaction (HER) catalysts due to their favourable synthesis conditions, stability, and high catalytic efficiency. We use a thermodynamic approach in conjunction with density functional theory and a kinetic model of exchange current density to systematically study the HER activity of β-Mo_2C under different experimental conditions. We show that the (011) surface has the highest HER activity, which is rationalized by its lack of strong Mo-based hydrogen adsorption sites. Thus, the HER efficiency of β-Mo_2C can be tuned using nanoparticles (NPs) that expose larger fractions of this termination. We give definite maps between NP morphologies and experimental synthesis conditions, and show that the control of carbon chemical potential during synthesis can expose up to 90% of (011) surface, while as H_2 ambient has little effect on NPs morphology. The volcano plot shows that under these optimum conditions, the NP exchange current density is $\sim 10^{-5}$ A/cm^2, that is only slightly smaller than that of Pt (111).

TABLE OF CONTENTS

LIST OF TABLES

LIST OF FIGURES

PREFACE

First, I would like to thank my thesis advisor Professor Wissam Saidi of the Swanson School of Engineering at University of Pittsburgh. He provided insight and expertise that greatly lead to the accomplishment of this research.

I would also like to acknowledge Professor Brian Gleeson and Professor Jung Kun Lee of the Swanson School of Engineering at University of Pittsburgh who gave me the opportunity to initiate my study and research in Mechanical Engineering and Materials Science program at University of Pittsburgh.

I am obliged to express my very profound gratitude to my parents, Yee-Pien Yang, Tzu Yuan Chang, and to my partner, Hsing Jung Wu, my friend Chein Wei Lin for providing me with unfailing support and continuous encouragement throughout my years of study and research. Such accomplishment would not have been possible without them. Thank you.

Finally, I praise the Lord for his glorious creation, grace and mercy. “All things were made by him; and without him was not any thing made that was made” (John 1:3).

Author

Timothy T. Yang

1.0 INTRODUCTION

The primary sources of energy are fossil fuels. In 2015, there were 32% of energy produced from natural gas, 28% from petroleum and 21% from coal in the nation recorded by U.S Energy Information Administration. Thus, it is always urgent to search for sustainable and environmentally benign energy sources which can replace for the diminishing fossil fuels. Among several renewable sources such as hydropower, biomass, biofuels, wind, geothermal and solar, hydrogen is considered as one of the important energy carrier because of its simplicity and abundance. Even high energy is generated thought combustion of pure hydrogen with oxygen with no harmful byproducts which are merely water and heat. However, more than 95% of H_2 gas is produced from unsustainable fossil fuels including steam methane reforming[1], partial oxidation of hydrocarbons[2], auto thermal reforming[3,4], coal gasification[5]and water-gas shift reaction[6]. In addition to their harmful environmental effects, these methods also suffer from low H_2 conversion efficiency, hydrogen purity, and carbon-based greenhouse gases emission.

The direct decomposition of water, or water electrolysis, is a promising alternative to traditional hydrogen production methods, which can alleviate most of the problems of traditional approaches.[7] Furthermore, hydrogen produced through electrolysis is also envisioned as a means for storing electricity in a form that can be easily redistributed and converted back into energy with no negative impact on environment. Among the discovered hydrogen evolution reaction (HER) catalysts, platinum is considered the best, but its high cost hampers commercial

applications.[8] This explains the active research in finding alternative earth-cheap materials with good catalytic efficiency towards HER. To this end, several potential candidates have been identified such as transition metal dichalcogenides[9], MoS_2[10-15],WS_2[16,17], MoP[18,19], nitrides[20,21], and molybdenum carbides[22,23].

1.1 WATERELECTROLYSIS

Water electrolysis is the chemical process of splitting water molecules into oxygen and hydrogen gas using electric current, and the generated hydrogen gas is collected as an energy carrier. There are three general approaches: the thermochemical water splitting, photobiological water splitting and photocatalytic water splitting.

The thermochemical water splitting drives series of chemical reactions to produce hydrogen at high temperature in the range of 500 ˚C to 2000 ˚C. For example, a three-step metal oxide cycle used for water splitting begins with the reduction of metal oxide such as Li_2O_2, Na_2O_2 and K_2O_2 [24] at high temperature accompanied with the product of oxygen gas. The reduced metal oxide than react with an alkali metal hydroxide to form mixed hydroxide and hydrogen. In the final step, the mixed hydroxide reacts with water to regenerate metal oxide and alkali metal hydroxide. The three-step metal oxide cycle can be written as:

$$MO_{ox} \rightarrow MO_{red} + \frac{1}{2}O_2$$

$$MO_{red} + 2M'OH \rightarrow M'_2O.MO_{ox} + H_2$$

$$M'_2O.MO_{ox} + H_2O \rightarrow MO_{ox} + 2M'OH$$

Therefore, the net reaction is

$$H_2O \rightarrow H_2 + \frac{1}{2}O_2$$

Sunlight or waste heat from nuclear reactors are used as the energy sources to run the cycles with nearly zero emission of green-house gases. However, such pathways of producing hydrogen still face challenges including the efficiency and durability of reactant materials for thermochemical cycling and the high cost of concentrating mirror systems.

Green microalgae and cyanobacteria are involved in the process of photobiological water splitting. These organisms adsorb sunlight as an energy source and use carbon dioxide as carbon source to produce hydrogen. There are two main ways to produce hydrogen using organic matters namely the photoautotrophic and photoheterotrophic hydrogen production. In normal photoautotrophic growth, the organic matters such as microalgae and cyanobacteria use sunlight and water substrate to metabolize carbon dioxide in the organic compounds $[C_n(H_2O)_n]$. However, when this process in under anaerobic conditions, microalgae can produce hydrogen by combining water with sunlight. The general process is an endothermic process with Gibbs free energy ΔG^0=1498 kJ:

$$4H_2O + solar\ energy \rightarrow 2O_2 + 4H_2$$

For photoheterotrophic production of H_2, the bacteria are catalyzed by nitrogenase enzyme through N_2 fixation. The overall energy consumption is written as

$$N_2 + 8H^+ + 8e^- + 16ATP \rightarrow 2NH_3 + H_2 + 16ADP + 16P_i$$

Such enzyme can utilize sunlight to produce hydrogen though the endothermic reaction with Gibbs free energy ΔG^0=75.2 kJ:

$$C_2H_4O_{2liq} + 2H_2O_{liq} + solar\ enegy \rightarrow 2CO_{2gas} + 4H_{2gas}$$

The challenge of photobiological water splitting is that the process is always accompanied with oxygen which lowers the hydrogen production rate and increases the risk to store hydrogen gas.

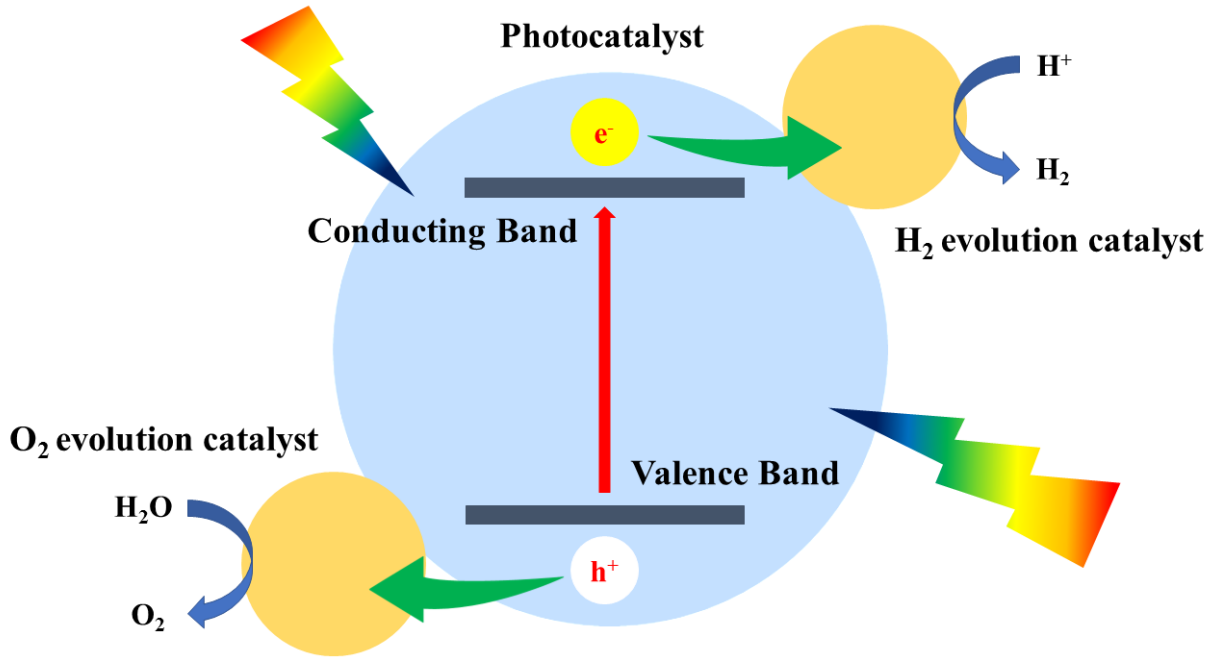

Figure 1. The scheme of a semiconductor photocatalyst. The process of hydrogen production undergoes three main steps: (1) electron-hole pairs are excited by light. (2) The electrons migrate into H_2 and O_2 evolution catalysts. (3) The hydrogen gas is generated by H_2 evolution catalysts, and the oxygen gas is generated by O_2 evolution catalysts.

Photocatalytic water splitting is another strategy to convert solar energy into hydrogen fuel via a low-cost way. It was first introduced by Honda and Fujishima who used titania electrode for photo electrochemical water splitting in 1972[25]. In addition to titania, there are several semiconducting materials that can bused for this reaction such as CdS[26] and g-C_3N_4[27] with a band gap energy of 2.7 eV. CdS has a bandgap of 2.4 eV which is suitable for solar spectrum, however it is not stable in aqueous solution due to photo corrosion. g-C_3N_4 has high heat resistance and is stable in acidic and alkaline solution, but the moderate bandgap of 2.7 eV makes it not very efficient to adsorb sunlight. The general process of photocatalytic water splitting is shown in **Figure 1**. These steps are (1) the generation of electron-hole pairs through exciting electrons from the valence band to conduction band after the lights are adsorbed by the

photocatalysts. (2) Migration of electrons and holes to the surface of semiconductor. (3) Production of hydrogen and oxygen gas using H_2 or O_2 evolution catalysts.

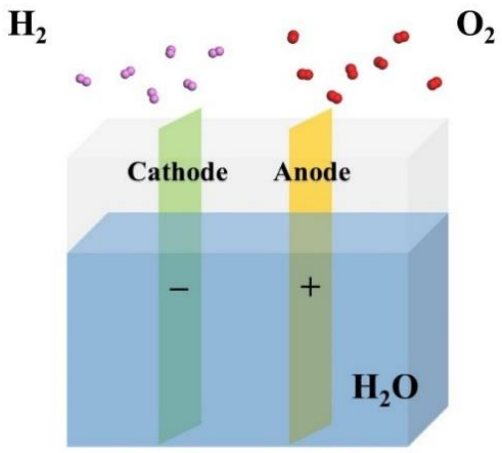

Figure 2. The scheme of an electrolyzer

An electrolyzer, which is used for hydrogen and oxygen production, is composed of an anode, a cathode and electrolyte, as shown in **Figure 2**. Note that pure H_2O is hard to be decomposed by electricity. Therefore, dilute sulfuric acid (H_2SO_4) or hydrochloric acid (HCl) is usually used as electrolyte After applying an external potential to the electrodes, water molecules in electrode are decomposed into oxygen and hydrogen followed by total reaction:

$$2H_2O_{(l)} \rightarrow +2H_{2(g)} + O_{2(g)}$$

At positively charged anode, oxygen gas is released into atmosphere through oxygen evolution reaction (OER); at negatively charged cathode, hydrogen gas is produced though hydrogen evolution reaction (HER). In acidic, neutral or basic solution, these gas evolutions undergo dissimilar pathways:

(In acidic solution)	(In basic or neutral solution)
Anode: $H_2O \rightharpoonup 2H^+ + \frac{1}{2}O_2 + 2e^-$	Anode: $2OH^- \rightharpoonup H_2O + \frac{1}{2}O_2 + 2e^-$
Cathode: $2H^+ + 2e^- \rightharpoonup H_2$	Cathode: $2H_2O + 2e^- \rightharpoonup H_2 + 2OH^-$

1.2 HYDROGEN EVOLUTION REACTION

Hydrogen evolution reaction (HER), the cathodic half reaction of water electrolysis, is generally believed to proceed through two consecutive sub-processes namely the Volmer reaction followed by Tafel or Heyrovsky reactions:

$$H^+ + e^- \rightarrow H^* \text{ (Volmer reaction)}$$

$$2H^* \rightarrow H_2 \text{ (Tafel Reaction)}$$

$$H^* + H^+ + e^- \rightarrow H_2 \text{ (Heyrovsky Reaction)}$$

In the Volmer reaction step, hydrogen atoms are adsorbed on the electrode surface by discharging protons with electrons transferred from electrode. When a hydrogen atom is adsorbed on the surface, it can interact with another adsorbed hydrogen to form hydrogen molecule via Tafel reaction, or directly with a proton via Heyrovsky reaction. The scheme of the three reactions is illustrated in **Figure 3**.

These reactions are stimulated by electron transfer between electrolyte and cathode usually made by high efficient heterogeneous catalysts such as platinum. Thus, the pathway of HER highly depends on the electronic property of catalysts. Markovic concluded that at Pt (110), the HER reaction follows Volmer-Tafel mechanism with Tafel reaction as determining reaction.

On the other hand, Pt (100) follows Volmer-Heyrovsky mechanism with Heyrovsky as rate determining step.[28] Later, Norskov suggested that both mechanisms can work in parallel on Pt (111) as the two pathways have similar activation energy.[29]

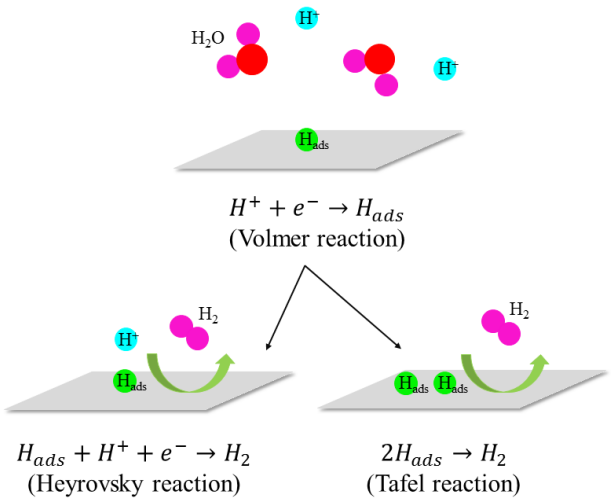

Figure 3. The hydrogen evolution reaction. Volmer reaction is followed by Heyrovsky or Tafel reaction.

1.3 MOLYBDENUM CARBIDE

Molybdenum carbides can be stable in two main Mo/C stoichiometries: 1:1 and 2:1. For MoC, the stable phases are hexagonal η-MoC and cubic δ-MoC at high temperatures above 1700˚C, while as the hexagonal γ-MoC is the stable phase at room temperature. On the other hand, for Mo_2C, the most stable structure is in the form of a disordered closed packed hexagonal structure (space group *P63/mmc*) above 1960˚C, and ε-Fe_2N-type hexagonal (space group *P3m1*) in

between 1350˚C and 1960˚C. Below 1350˚C, ζ-Fe_2N-type orthorhombic structure is the most stable one. The phase diagram of these structures is shown in **Figure 4**, and the atomic structures of the common phases are shown in **Figure 5**.

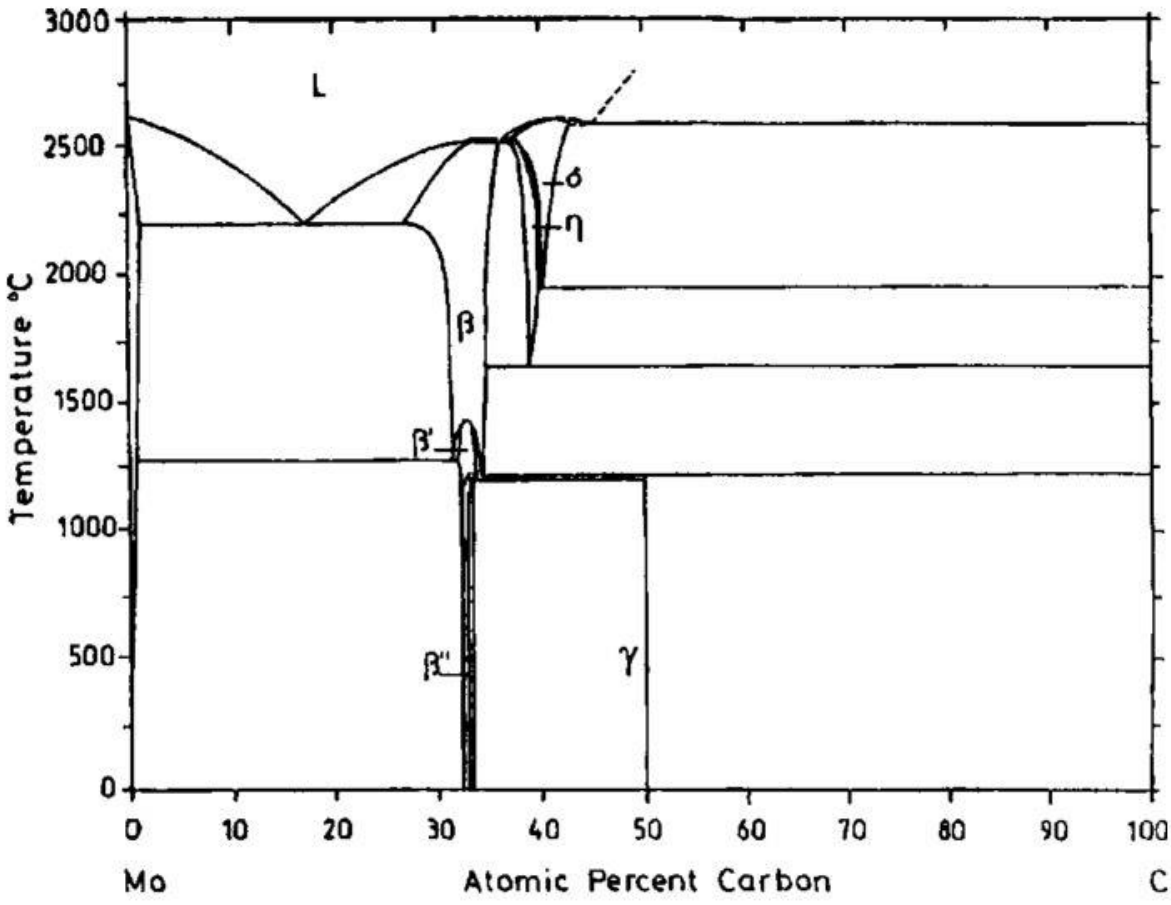

Figure 4. The phase diagram of molybdenum carbide and the structures of different phases. Reference: Hugosson, H. k. W. et al. Journal of Applied Physics 86, 3758 (1999).

The orthorhombic and the closed packed hexagonal Mo_2C are synthesized using different methods [30-34], but structurally they are very similar, which explains why these are used interchangeably in several studies[35-38]. For consistency, we always refer to the orthorhombic structure as α-Mo_2C and the hexagonal structure as β-Mo_2C. Haines[39] proposed a disordered

hexagonal structure for β-Mo_2C, which Shi et al.[40] later refined using density functional theory (DFT) calculations by considering all arrangement possibilities of carbon atoms at octahedral sites as shown in **Figure 6**. This study showed that the structure in **Figure 6 (e)** (or **Figure 7**) has the lowest energy, which has been employed in other studies [41-43].

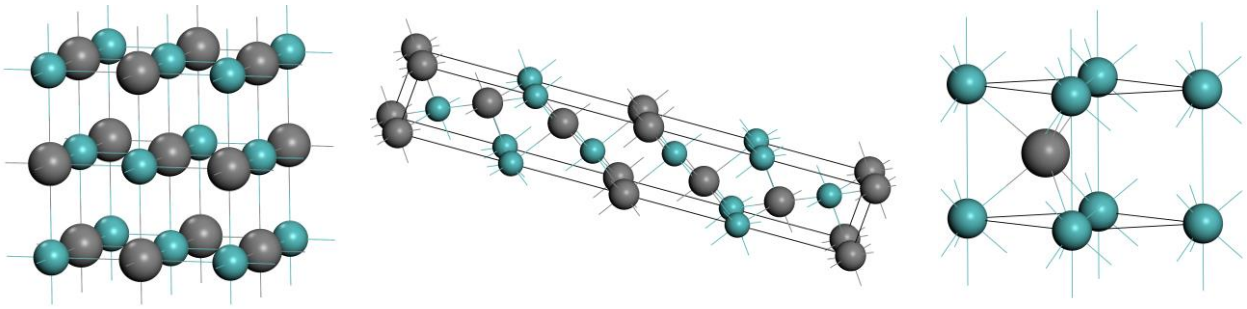

Figure 5. δ-MoC (left), η-MoC (middle), and γ-MoC (right).

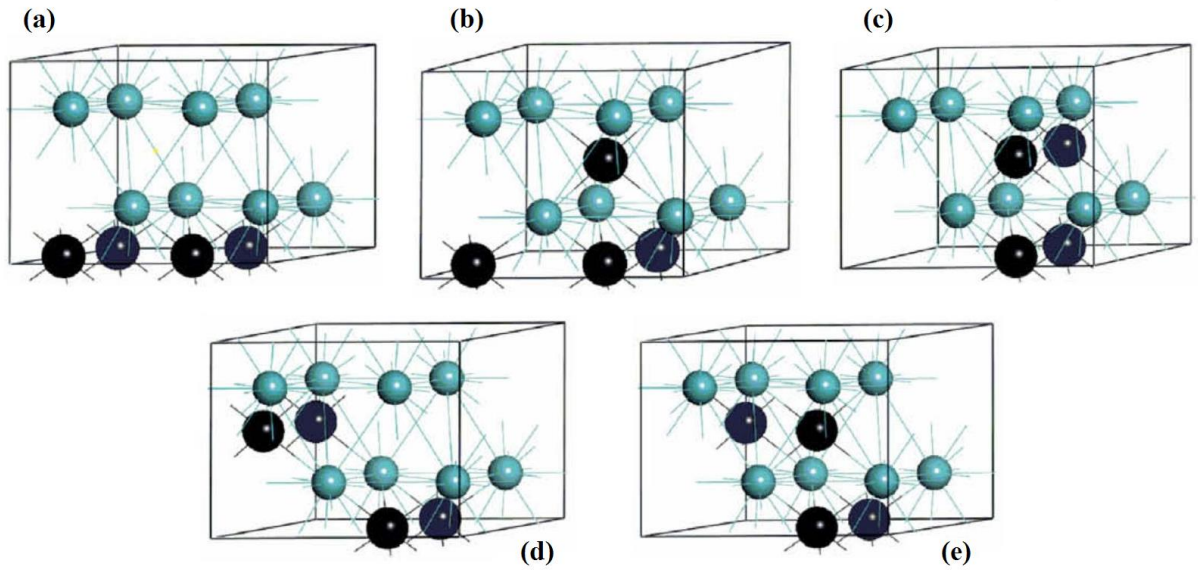

Figure 6. Five possible hexagonal β-Mo_2C structures with disordered carbon atoms at octahedral sites tested by Shi. The down-right one has the lowest energy, and is considered to be the most possible hexagonal β-Mo_2C structure. Reference: Shi, X.-R. et al. Surface Science (2009).

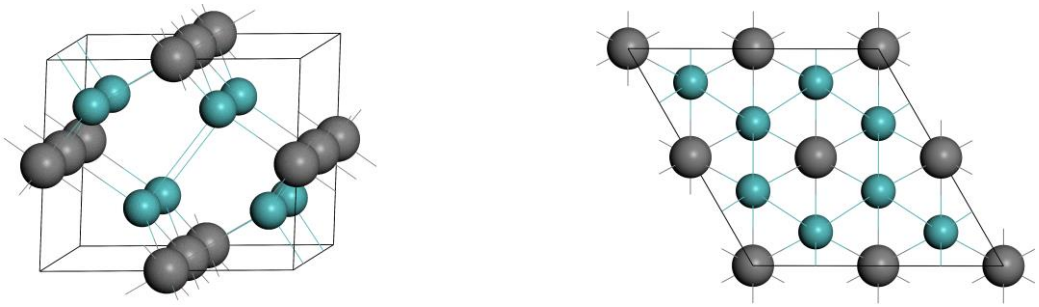

Figure 7. The side and top view of hexagonal β-Mo_2C structure.

1.4 MOTIVATION AND RESEARCH OBJECTIVES

In a recent study, Wan and collaborators investigated different phases of MoC and Mo_2C (**Figure 8**), and showed that the β-Mo_2C phase exhibited superior HER activity (**Figure 9**).[36] Others demonstrated that β-Mo_2C catalyst is flexible and can be employed as unsupported nanoparticles (NPs)[44], or as supported NPs on carbon nanotubes[45,46], graphene[47], and graphene oxide[48], or in even more complex forms as nitrogen-doped carbon nanotube embedded with β-Mo_2C[49]. These studies suggest that the catalytic efficiency of β-Mo_2C is sensitive to several variations, and accordingly can be tailored, e.g. by tuning surface termination, shape and support. Indeed, it was previously shown that α-Mo_2C, which is similar in structure to β-Mo_2C, has a catalytic activity that is sensitive to the surface terminations: the water-gas shift reaction on (001) C terminated surface has a better activity than the (001) Mo terminated surface[50], while as the opposite is true for the hydrogenation of CO_2 to methanol and methane[51]. To date, the atomistic mechanism of HER activity on β-Mo_2C has not been explored. Therefore, a deeper understanding of β-Mo_2C and its electronic structure is required for systematic improvement of

catalytic efficiency. In this research, we demonstrate the paradigm for HER dependence on morphologies of β-Mo_2C NPs, and we give definite maps showing how the control of the carbon chemical potential during β-Mo_2C synthesis can affect the morphology of NPs and its exchange current density.

We use a thermodynamic approach in conjunction with density functional theory (DFT) and a kinetic model of exchange current density[52] to delineate different experimental boundary conditions of NPs synthesis and HER measurements. The exchange current density assumes that hydrogen adsorption free energy is a good descriptor to HER activity. This model was successfully applied to different systems such as MoS_2[53], CdS, ZnS[54], VS_2 nanoribbon[55], doped Co NPs[56], and WC-supported metal monolayers[23,57]. The strength of this approach is that it provides a good approximation for the HER activities without considering kinetic aspects or detailed processes.

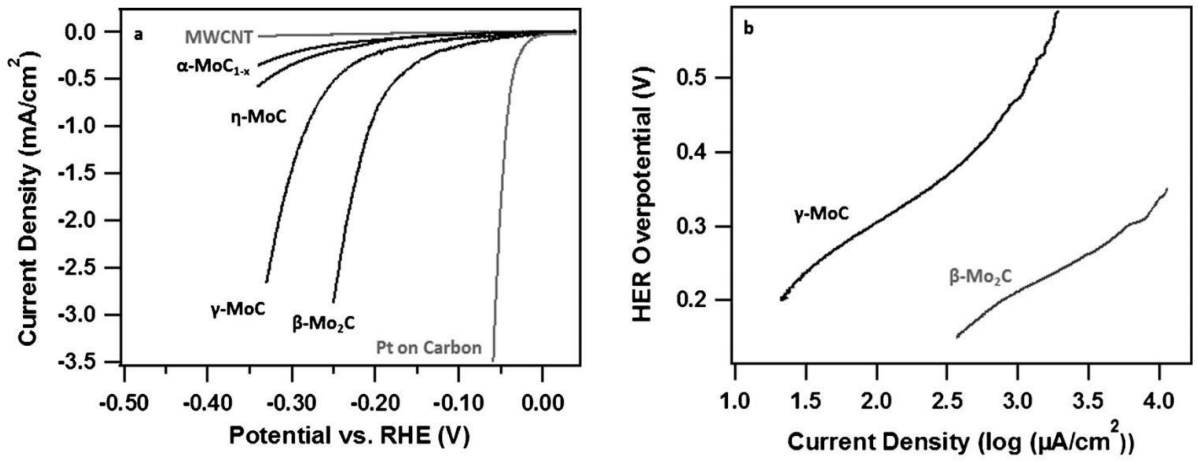

Figure 8. Wan et al. Compare HER activity on four different phases, and β- Mo_2C shows the highest HER activity among the other phases. *Reference: Wan, C. et al. Angew Chem Int Ed Engl 53, 6407-6410 (2014).*

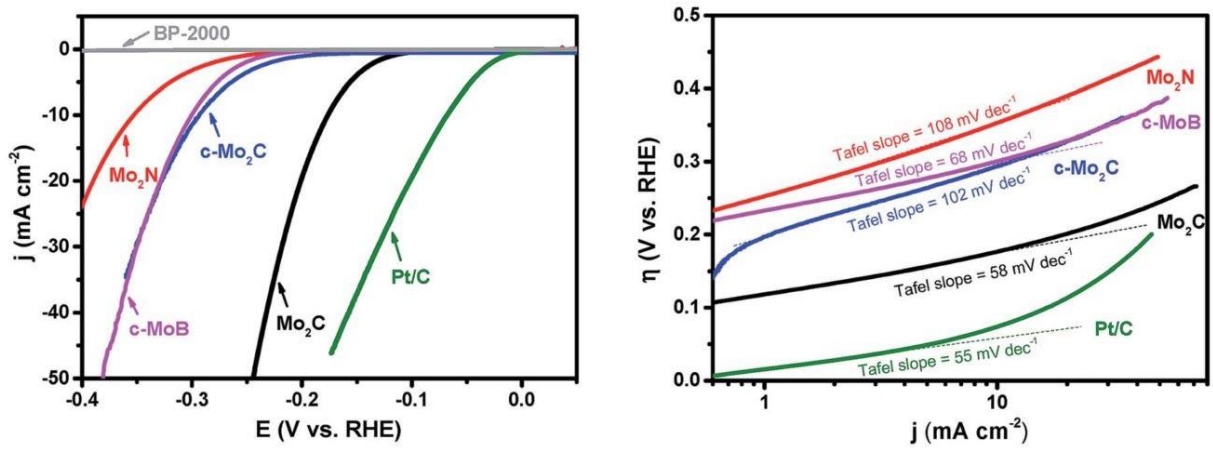

Figure 9. Ma et al. compares HER activity on few catalysts. The experiment shows good HER activities on commercial Mo_2C (c-Mo_2C) and Mo_2C synthesized via urea glass route.

2.0 THEORETICAL APPROACHES

To study hydrogen evolution on β-Mo_2C, we use a thermodynamic approach in conjunction with density functional theory to study hydrogen evolution reaction at 298K and Mo_2C synthesis at 1000K. In this chapter, we will first introduce the basics of density functional theory, and will discuss the hydrogen adsorption and surface stability at finite temperature using thermodynamics.

2.1 DENSITY FUNCTIONAL THEORY

For a single particle system, all of the system information is contained in a wavefunction $\Psi(x,t)$ which depends on position x and time t. The wavefunction satisfies the Schrodinger Equation

$$i\hbar\frac{\partial\Psi(x,t)}{\partial t} = -\frac{\hbar^2}{2m}\frac{\partial^2\Psi(x,t)}{\partial x^2} + V\Psi(x,t)$$

where $\hbar$ is Planck constant, m is the mass of that particle and V is potential the particle is experienced. For time-independent potentials, the wavefunction can be expressed as a linear combination of time-independent state functions $\varphi_n(x)$

$$\Psi(x,t) = \sum_n c_n\varphi_n(x)e^{-iE_nt/\hbar}$$

For state n, the eigen state energy E_n, and with Hamiltonian operator

$$\hat{H} = -\frac{\hbar^2}{2m}\frac{\partial^2}{\partial x^2} + V$$

the allowed energies can be simply described as an eigenequation

$$\hat{H}\varphi_n(x) = E_n\varphi_n(x)$$

For a many-body system contains N_N nuclei and N_E electrons, the system's wavefunction Ψ_n satisfies

$$\hat{H}\Psi_n(r_1, r_2, r_3 \dots r_{N_E}, R_1, R_2, R_3 \dots R_{N_N}) = E_n\Psi_n(r_1, r_2, r_3 \dots r_{N_E}, R_1, R_2, R_3 \dots R_{N_N})$$

where r_i and R_i are the electrons and nuclei positions, and the Hamiltonian operator is

$$\hat{H} = -\frac{1}{2}\sum_{i=1}^{N_E}\nabla_{\mathrm{i}}^2 - \frac{1}{2}\sum_{i=1}^{N_N}\frac{1}{M_{N_N}}\nabla_{\mathrm{i}}^2 - \sum_{i=1}^{N_E}\sum_{j=1}^{N_N}\frac{Z_{N_N}}{r'_{ij}} + \sum_{i\neq j}^{N_E}\frac{1}{r_{ij}} + \sum_{i\neq j}^{N_N}\frac{Z_iZ_j}{R_{ij}}$$

The first two terms are the kinetic energy of elections, and the last three terms are the coulomb potential from electron-nucleus interaction, electron-electron interaction and nucleus-nucleus interaction. Because the mass of nuclei is much larger than the mass of electrons, the nuclei can be assumed fixed in position, which is known as Born-Oppenheimer approximation. In this case, the Hamiltonian operator can be simplified to

$$\hat{H}_E = -\frac{1}{2}\sum_{i=1}^{N_E}\nabla_{\mathrm{i}}^2 - \sum_{i=1}^{N_E}\sum_{j=1}^{N_N}\frac{Z_{N_N}}{r'_{ij}} + \sum_{i\neq j}^{N_E}\frac{1}{r_{ij}} = \hat{T} + \hat{V}_{NE} + \hat{V}_E$$

Here V_{NE} descibes the coulomb interactions between nuclei and electrons and V_E is the coulomb potential between electrons. The eigenvalues E_E and eigenfunctions Ψ_{E} satisfy

$$\hat{H}_E\Psi_{\mathrm{E}} = E_E\Psi_{\mathrm{E}}$$

Originally, these many body equations are solved using mean field theories such as Hartree-Fock. However, they are generally poor in approximating of many-body systems. Higher order theories building on the Hartree Fock solutions were also introduced such as MP2, MP4 and

coupled cluster, which can solve many-body problems more accurately. These approaches are mostly employed in the quantum chemistry community, and are computationally very expensive.

Density functional theory is a method to solve the Schrodinger equation for a many-body system which was introduced by Kohn, Hohenberg, and Sham. To avoid using many body wave function that solves the Schrodinger equation, this approach requires only the electron charge density, which depends on three coordinates, to know all the properties of a system. Thus, the total energy of a system is only a functional of electron density. The electron density can be obtained from the many body wavefunction using

$$n(\vec{r}_1) = N \int d^3r_2 \dots \int d^3r_3 \dots \int d^3r_n \, \Psi^*(\vec{r}_1, \vec{r}_2 \dots \vec{r}_N)\Psi(\vec{r}_1, \vec{r}_2 \dots \vec{r}_N)$$

If we consider the energy function does not explicitly depend on the electron-electron interaction, we can rewrite the electronic Hamiltonian operator as

$$\hat{H}_s = \hat{T} + \hat{V}_{NE} + \hat{V}_E = \hat{T} + \hat{V}_s$$

The universal operator $\hat{T}$ and $\hat{V}_E$ are the same for every system. Whereas, external potential $\hat{V}_{NE}$ is unique for different systems. The expectation value of the energy is

$$E_s[n] = \langle \Psi_s[n] | \hat{T} + \hat{V}_s | \Psi_s[n] \rangle$$

Using the variational principle in quantum mechanics, for any normalized wavefunction $\Psi_s[n]$ that is not true eigenstate for a corresponding Hamiltonian, the expectation energy of such wavefunction gives the upper bound of the true ground state energy $E_s[n_s]$ of that system,

$$E_s[n_s] \leq \langle \Psi_s[n] | \hat{T} + \hat{V}_s | \Psi_s[n] \rangle$$

If the true electron density n_s gives the true wavefunction $\Psi_s[n_s]$ of a many-body system, one can solve the Kohn-Sham equation,

$$-\frac{\hbar^2}{2m}\nabla^2\Psi_s[n_s] + \hat{V}_s\Psi_s[n_s] = E_s[n_s]\Psi_s[n_s]$$

Also, the electron density is related to the wavefunction,

$$n_s = \sum_i^N |\Psi_s[n_s]|^2$$

and the effective single-particle potential can be expressed as

$$V_s(\vec{r}) = V(\vec{r}) + \int \frac{e^2 n_s(\vec{r}')}{|\vec{r} - \vec{r}'|} d^3r' + V_{XC}[n_s(\vec{r})]$$

Here, the first term on the right side of the equation is the potential between electrons and nuclei. The second term is called Hartree potential, which includes the Coulomb interactions of all electrons. The last term is the exchange-correlation potential, which contains all the other particle interactions beyond the mean field Hartree interactions. It can be related to exchange correlation energy as

$$V_{XC}[n_s(\vec{r})] = \frac{\delta E_{XC}(n_s(\vec{r}))}{\delta n_s(\vec{r})}$$

The exchange correlation functional depends on the electron density, but its actual form is unknown. There are different approximations for the exchange correlation functional, and the most common approximations are the local density approximation (LDA) and gradient approximation (GGA). LDA is based on the assumption that the homogeneous electron gas is uniformly distributed in space, that is

$$E_{XC}^{LDA} = \int \varepsilon_{XC}^{hom}(\vec{r}) n_s(\vec{r}) d\vec{r}$$

In reality, the electron gas is inhomogeneous in space, therefore LDA is not as accurate as GGA where the effects of inhomogeneities are considered by including the gradient of the electron density. The GGA can be written as

$$E_{XC}^{GGA}[n_s(\vec{r})] = \int n_s(\vec{r})_{XC}^{hom}[n_s(\vec{r})] F_{XC}[n_s(\vec{r}), \nabla n_s(\vec{r})] d\vec{r}$$

where $F_{XC}[n(\vec{r}), \nabla n(\vec{r})]$ is call the enhancement factor. In computational algorithm, the total energy of the system is found by the following steps:

1. Define a trial electron potential $n(\vec{r})$
2. Use $n(\vec{r})$ to solve Kohn-Sham equation to find the wavefunction $\Psi_s[\, n(\vec{r})]$
3. Calculate the electron density from the wavefunction found step 2

$$n'(\vec{r}) \; = \sum_{i}^{N} |\Psi_s[n(\vec{r})\,]|^2$$

4. Compare $n'(\vec{r})$ and $n(\vec{r})$: if the two electron densities are the same, $n'(\vec{r})$ will be used to compute the total energy. If the two electron densities are not the same, the trial electron density $n(\vec{r})$ will be redefined, and the process will be resumed.

2.2 HYDROGEN ADSORBED GIBBS FREE ENERGY

When hydrogen molecules in gas phase are adsorbed on surface, they form bonds with the surface atoms and release an amount of energy to stabilize the system. Reversibly, for hydrogen atoms to leave the surface as hydrogen gas, the same amount of energy is required to break the bonds. (For such statement, we exempt out the effect of kinetic barriers) Therefore, we defined the *DFT averaged hydrogen adsorption energy* as

$$\Delta E_{\mathrm{H}^*} = \frac{1}{n}(E_{\mathrm{slab/H}} - E_{\mathrm{slab}} - n\frac{1}{2}E_{\mathrm{H_2}})$$

where n is the number of adsorbed hydrogen atoms, $E_{\mathrm{slab/H}}$ and E_{slab} are the energy of the slab with n adsorbed hydrogen and of the clean slab respectively. $E_{\mathrm{H_2}}$ is the energy of a hydrogen

molecule in gas phase. We use an *ab initio* thermodynamic[58] approach to compute the hydrogen adsorption Gibbs free energy (at finite T and pressure) as

$$\Delta G_{\mathrm{H}^*} = \frac{1}{n}(G_{\mathrm{slab/H}} - G_{\mathrm{slab}} - n\frac{1}{2}G_{\mathrm{H_2}})$$

where $G_{\mathrm{slab/H}}$ and G_{slab} are the Gibbs free energy of the slab with and without hydrogen, which are approximated from Helmholtz free energy $G(T,p) \approx F(T,V)$ by ignoring pV. $F(T,V)$ is defined as

$$F(T,V) = E_{\mathrm{DFT}} + E_{\mathrm{vib}} - TS_{\mathrm{vib}}$$

where E_{DFT} is DFT energy, E_{vib} and S_{vib} are vibrational energy and entropy

$$E_{vib} = \frac{1}{2}\sum_i h\nu_i + \sum_i \frac{h\nu_i e^{-h\nu_i/(k_\beta T)}}{1 - e^{-h\nu_i/(k_\beta T)}}$$

$$S_{vib} = k_\beta \sum_i \left(\frac{h\nu_i}{k_\beta T}\right)\frac{e^{-h\nu_i/k_\beta T}}{1 - e^{-h\nu_i/k_\beta T}} - k_\beta \sum_i \ln(1 - e^{-\frac{h\nu_i}{k_\beta T}})$$

Here, ν_i is the phonon frequency, and k_β is Boltzmann constant. The Gibbs free energy of H_2 in the gas phase, which depends on temperature T and the hydrogen partial pressure p_{H_2}[59] as a reference to standard state pressure p^θ is defined as

$$G_{H_2} = E_{H_2} + \tilde{\mu}_{H_2}(T, p^0) + k_B T ln\left(\frac{p_{H_2}}{p^0}\right)$$

$$\tilde{\mu}_{H_2} = [H(T,p^0) - H(0,p^0)] - T[S(T,p^0) - S(0,p^0)]$$

We have implied the basic relation in thermodynamics, $G = H - TS$, to express $\tilde{\mu}_{H_2}$ with enthalpy H and entropy S as a reference to zero temperature at 1 atm. $H(T,p^0)$ and $S(T,p^0)$ for all temperatures are obtained from NIST-JANAF thermochemical tables[59]. In the limit of zero temperature, the adsorbed Gibbs free energy can be calculated by DFT defined as

$$\Delta G_{H^*} = \Delta E_H + \Delta E_{ZPE}$$

The zero-point energy ΔE_{ZPE} is the difference of hydrogen vibrational energy between adsorbed and gas phase at zero temperature.

2.3 THE SURFACE FREE ENERGY

The surface free energy is the work required to create surface. The surface stability is gauged by inspecting the surface free energy defined as

$$\gamma_{\text{surf}} = \frac{1}{2A}(G_{\text{slab}} - N_{\text{Mo}}\mu_{\text{Mo}} - N_{\text{C}}\mu_{\text{C}})$$

where N_i (i=Mo, C) is the number of atoms, μ_{i} is chemical potential, and A is exposed surface area. To eliminate the dependence on Mo chemical potential, we can simplify the equation to

$$\gamma_{\text{surf}} = \frac{1}{2A}\left(G_{\text{slab}} - \frac{N_{\text{Mo}}G_{\text{bulk}}}{2} + \frac{(N_{Mo} - 2N_C)}{2}\mu_C\right)$$

To calculate the surface free energy of these non-stoichiometric models, we keep the atoms in the middle layers of the slabs fixed in bulk position, and relax the atoms in top and bottom layers. For models with the same terminations on the top and the bottom of the slabs, γ_{surf} is an averaged value from the two equivalent surfaces. We verified that our results are equivalent to the surface energies $\gamma_{\text{surf}} = 2\gamma_{\text{surf (Relaxed)}} - \gamma_{\text{surf (Fixed)}}$, where $\gamma_{\text{surf (Relaxed)}}$ is the surface free energy of a slab with bottom half atoms fixed in bulk position and $\gamma_{\text{surf (Fixed)}}$ is the surface free energy of a slab with all the atoms fixed in bulk position. In the presence of hydrogen, the surface energy is written as

$$\gamma_{\text{surf}}^{\text{H}_2} = \gamma_{\text{surf}} + \gamma_{\text{H}_2} \quad \text{and} \quad \gamma_{H_2} = \frac{1}{2A}(n\Delta G_{\text{H}^*})$$

where ΔG_{H^*} is the hydrogen adsorption energy defined previously.

3.0 COMPUTATIONAL APPROACH AND VALIDATION

In this chapter, we will provide the computational setups of using Vienna Ab Initio Simulation Package (VASP) for the calculations based on density functional theory (DFT). We will also discuss the models we use for these simulations. We thoughtfully check that our setups are valid for our work.

3.1 COMPUTATIONAL DETAILS

The first-principle calculations are based on density functional theory (DFT) as implemented in the Vienna Ab Initio Simulation Package (VASP)[60]. We employ the Perdew-Burke-Ernzerhof (PBE) exchange-correlational functional[61] to solve the Kohn-Sham equations within periodic boundary conditions. (We carry out additional calculations for the hydrogen binding energy using RPBE on the (011) surface. Our PBE and RPBE results are shown in **Table 1**. As can be seen, the difference between the PBE and RPBE absolute binding energies is small, less than 0.11 eV.).

The electron-nucleus interactions are described using PAW pseudopotentials.[62,63] The Monkhorst-Pack *k*-point is set to 4 × 4 × 4 for bulk optimization and 4 × 4 × 1 in calculations of slab systems. The partial occupancies of the bands are determined using the first-order scheme of

the Methfessel-Paxton method with a 0.05 eV width. We used a planewave cutoff of 400 eV, which was verified to be large enough as using a smaller cutoff of 300 eV changes energy differences by less than 3%. The electronic self-consistent loop is terminated when energy changes are less than 1×10^{-5} eV and the ionic relaxations are considered converged when the magnitude of the largest force on any atom is less than 0.01 eV/Å. Using this computational setup, we find that the optimized hexagonal β-Mo_2C unit cell has dimensions 6.061 × 6.054 × 4.713 $Å^3$, which is in good agreement with previous DFT/RPBE results[40] 6.051 × 6.048 × 4.732 $Å^3$, as well as with experimental results[30] 6.0248 × 6.0248 × 4.7352 $Å^3$.

To determine the equilibrium β-Mo_2C NPs morphology according to Wulff construction scheme, we investigated polar and non-polar polar low Miller index surfaces, which are obtained from bulk using a (1 × 1) surface supercell with 6 atomic layers for (011), (101), (110), 8 for (021), 18 for (100), 12 for (001) surface, 6 for (111) and 18 for (010). The fictitious interactions between images along the non-periodic direction are mitigated using 10 Å vacuum. We have verified that our results are not sensitive to slab thickness as summarized in **Table 2**. Further, we show in **Table 3** that our hydrogen adsorption Gibbs free energies on (001), (100) and (011) surfaces are in good agreement with previous DFT calculations[41].

Table 1. The *averaged hydrogen adsorption energy* calculated using PBE and RPBE functionals.

H Coverage	1	2	3	4	5	6	7	8
PBE (eV)	-0.58	-0.61	-0.49	-0.43	-0.35	-0.30	-0.28	-0.25
RPBE (eV)	-0.47	-0.50	-0.38	-0.32	-0.24	-0.19	-0.17	-0.14

Table 2. Surface free energies (J/m^2) calculated from 2 layer slabs and 3 layer slabs. Results show the convergence in energies for DFT calculations.

	(011)	(101)	(110)	(021)	(100)-C	(100)-Mo	(001)-C	(001)-Mo	(111)	(010)
2-Layer	3.138	3.116	3.363		3.376	3.396	3.382	3.496		
3-Layer	3.140	3.116	3.375	3.255	3.367	3.390	3.377	3.489	3.255	3.023

Table 3. The comparison of hydrogen adsorption energy in (eV) for four surfaces at hydrogen coverages. For each surface, the first row shows the reported energies in reference[41], and the second column is the energies calculated in our work. Note that (100) and (001) are Mo-terminated surfaces.

	1H	2H	3H	4H	5H	6H	7H	8H	9H	10H	11H	12H	13H	14H
(011)	-0.650	-0.612	-0.522	-0.470	-0.383	-0.339								
	-0.608	-0.628	-0.506	-0.453	-0.373	-0.317								
(100)	-0.995	-0.998	-0.873	-0.816	-0.677	-0.594								
	-0.963	-0.949	-0.870	-0.828	-0.703	-0.613								
(001)	-1.120	-1.119	1.011	-0.979	-0.800									
	-1.100	-1.113	-1.008	-0.984	-0.765									
(021)	-1.020	-0.967	-0.930	-0.919	-0.868	-0.815	-0.741	-0.680	-0.626	-0.595	-0.551	-0.512	-0.482	-0.455
	-0.989	-0.984	-0.933	-0.949	-0.949	-0.837	-0.762	-0.712	-0.655	-0.637	-0.592	-0.551	-0.521	-0.500

3.2 SLAB MODELS

The bulk β-Mo_2C with a hexagonal structure proposed by Shi et al is employed[40], and the slabs are modeled using a supercell approach with 6-18 atomic layers. The top and the bottom layers of the slab models are chosen to have the same termination, which make the slabs non-stoichiometric in the ratio of Mo and C. We investigate ten non-stoichiometric surfaces which are chosen from the most prevalent terminations in XRD measurements[36,64], in addition to the terminations with low surface free-energies[40]. Our selection includes four non-polar surfaces: (011), (101), (110), (021); two C-terminated polar surfaces: (100)-C, (001)-C; and four Mo-

terminated polar surfaces: (100)-Mo, (001)-Mo, (010)-Mo, (111)-Mo. These non-stoichiometric models have varying composition with Mo:C ratio of 1:1 for (011), 2:1 for (101) and (110), and 4:1 for (021). The (100)-C, (100)-Mo and (010)-Mo surfaces have a top C layer followed by two Mo layers, while (001)-C, (001)-Mo and (111)-Mo surfaces have alternating Mo/C layers. All surface terminations are cleaved in the most stable way as shown in **Figure 10.**

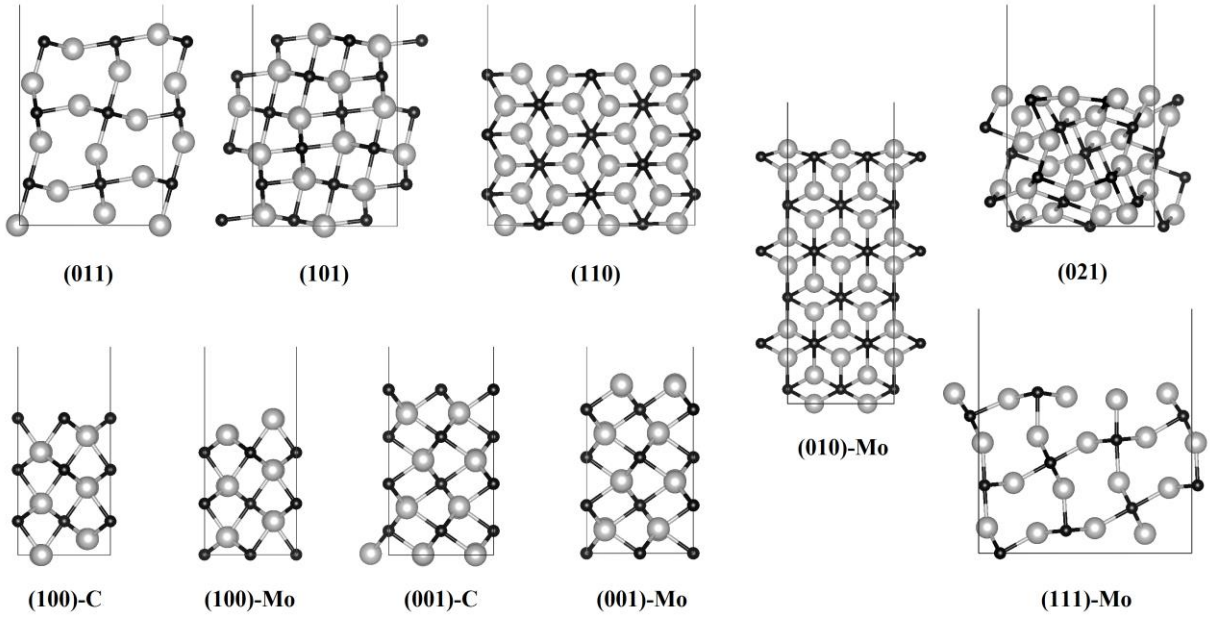

Figure 10. The side view of ten β-Mo_2C surfaces. The Molybdenum atoms and the Carbon atoms are in gray and black. Number of layers shows on the picture is used in actual DFT calculation.

4.0 HYDROGEN ADSORPTION

To unravel the high efficiency of hydrogen evolution reaction on β-Mo_2C nanoparticles, we investigate the hydrogen adsorption on β-Mo_2C and its correlation to atomic topology and electronic structure. We first use density functional theory to analyze the mechanism of hydrogen adsorption, which includes (1) the study of *hydrogen adsorption Gibbs free energy*, (2) the Bader charge analysis and (3) the *density of states* of β-Mo_2C surfaces. We further extend our investigations to finite temperature and pressure conditions to connect with experiments. We find that the high HER activity comes from mainly by exposing (011) surface which has a special electronic structure and can interact with hydrogen neither too strongly nor too weakly.

4.1 HYDROGEN ADSORPTION CONFIGURATION AT ZERO TEMPERATURE

The turn-over-frequency is proportional to the number of catalytic sites. For HER, these sites are determined by the most stable hydrogen adsorption configuration with the lowest hydrogen adsorption Gibbs free energy ΔG_{H^*} (at Zero Temperature) at a fixed hydrogen coverage *n*H, among all possible arrangements. For non-polar surfaces, we find that the most stable arrangement at (*n*+1)H hydrogen coverage can be obtained from the optimum configuration at *n*H hydrogen coverage by inspecting the energy of the system with an additional hydrogen atom

at all possible adsorption sites. However, this simple prescription failed for some polar surfaces, where in this case, we consider all possible symmetric arrangements of adsorbed hydrogen. In **Figure 12** to **Figure 21**, we show the hydrogen adsorption sites on ten different surfaces investigated as function of hydrogen converge.

Our findings of adsorption sites and energies on (011), (021), (100)-Mo, (001)-Mo surfaces by employing (1 × 1) surface supercells are in agreement with a previous study[41] that employed (2 × 1) supercells for (011), and (2 × 2) for (100)-Mo and (001)-Mo and (021). This indicates that hydrogen adsorption configurations are not sensitive to the supercell size. (Note that the (101) and (201) in Ref. 41 are respectively equivalent to (011) and (021) in our work.).

In our calculation of ΔG_{H^*}, we include the zero-point energy ΔE_{ZPE} of adsorbed hydrogen atoms and hydrogen molecule in vacuum. We ignore the vibration of the slabs because our calculation shows a negligible effect of less than 10^{-3} eV. This will be discussed in the later section of surface stability. The detailed values of zero-point energy contribution for each surface and for the investigated hydrogen coverages are included in **Table 5**.

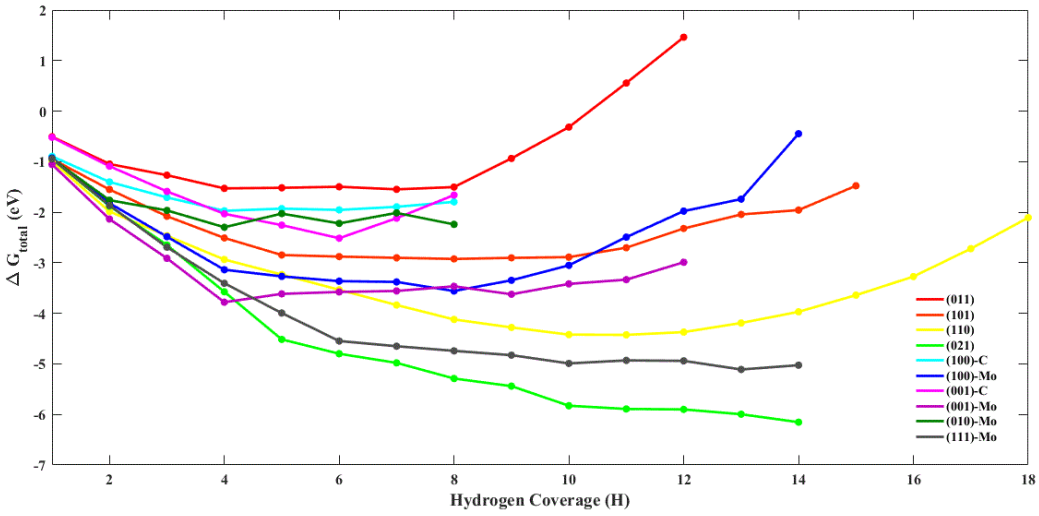

Figure 11. The total DFT averaged hydrogen adsorption energy of the ten surfaces.

Table 4. The *total DFT averaged hydrogen adsorption energy* ΔG_{total} (eV) of the ten surfaces at each hydrogen coverage (H)

	(011)	(101)	(110)	(021)	(100)-C	(100)-Mo	(001)-C	(001)-Mo	(010)-Mo	(111)-Mo
1H	-0.51	-0.95	-0.99	-0.95	-0.89	-0.93	-0.52	-1.06	-0.95	-0.94
2H	-1.05	-1.55	-1.99	-1.88	-1.40	-1.82	-1.09	-2.14	-1.87	-1.76
3H	-1.27	-2.08	-2.47	-2.65	-1.71	-2.48	-1.59	-2.91	-2.69	-1.96
4H	-1.53	-2.51	-2.94	-3.57	-1.97	-3.14	-2.03	-3.78	-3.41	-2.30
5H	-1.52	-2.85	-3.23	-4.52	-1.93	-3.27	-2.26	-3.61	-3.99	-2.03
6H	-1.50	-2.88	-3.54	-4.80	-1.96	-3.36	-2.51	-3.58	-4.55	-2.22
7H	-1.55	-2.90	-3.84	-4.98	-1.89	-3.38	-2.12	-3.56	-4.65	-2.01
8H	-1.50	-2.92	-4.12	-5.29	-1.80	-3.56	-1.66	-3.47	-4.74	-2.24
9H	-0.94	-2.90	-4.28	-5.44		-3.35		-3.62	-4.83	
10H	-0.32	-2.89	-4.42	-5.83		-3.05		-3.42	-4.99	
11H	0.55	-2.70	-4.43	-5.89		-2.49		-3.33	-4.93	
12H	1.46	-2.32	-4.37	-5.90		-1.98		-2.99	-4.94	
13H		-2.04	-4.19	-6.00		-1.74			-5.11	
14H		-1.96	-3.97	-6.15		-0.45			-5.03	
15H		-1.48	-3.64							
16H			-3.27							
17H			-2.72							
18H			-2.11							

The saturated hydrogen coverage is determined by the *total hydrogen adsorption Gibbs free energy* ΔG_{total}. It is defined as the sum of the *hydrogen adsorption Gibbs free energy,* ΔG_{H^*}, for all adsorbed hydrogen atoms in the system. That is, the total energy required to make all adsorbed hydrogen atoms on surface into hydrogen molecules in vacuum. When $(n+1)\Delta G_{\mathrm{H}^*} > n\Delta G_{\mathrm{H}^*}$, the n^{th} hydrogen configuration is more stable than the $(n+1)^{th}$ hydrogen configuration, therefore the system is saturated at n^{th} configuration. **Figure 11** shows ΔG_{total} of the ten surfaces and **Table 4** lists the detailed values. Note that in some of the surfaces, ΔG_{total} wiggles up and down around a small value in a range of hydrogen coverage. In this case, we can say that the system with these of hydrogen coverages is about equally stable, and it is possible for hydrogen

to be adsorbed in these hydrogen configurations. For example, for (011) surface, the system satisfies the condition of $(3+1)\Delta G_{\mathrm{H}^*} < 3\Delta G_{\mathrm{H}^*}$ at 4H coverage. However, ΔG_{total} from 4H and 8H are very similar, and the system can be stable at any of these coverages from 4H to 8H. These small variations may come from the uncertainties in our calculation. Such situation is also obvious on (101) surface from the hydrogen coverage of 5H to 10H hydrogen coverage, (100)-C surface from 4H to 8H, (100)-Mo surface from 6H to 9H, (001)-Mo surface from 7H to 9H and (111)-Mo surface from 10H to 13H.

Table 5. The *zero-point energy* of the ten surfaces at each hydrogen coverage.

	(011)	(101)	(110)	(021)	(100)-C	(100)-Mo	(001)-C	(001)-Mo	(010)-Mo	(111)-Mo
1H	0.10	0.04	0.04	0.04	0.12	0.03	0.11	0.04	0.04	0.05
2H	0.10	0.04	0.04	0.05	0.10	0.04	0.07	0.05	0.03	0.05
3H	0.08	0.03	0.04	0.05	0.09	0.04	0.05	0.04	0.05	0.04
4H	0.07	0.05	0.04	0.06	0.09	0.04	0.06	0.04	0.05	0.04
5H	0.07	0.05	0.05	0.05	0.10	0.05	0.08	0.04	0.05	0.04
6H	0.07	0.06	0.06	0.04	0.10	0.05	0.08	0.05	0.06	0.04
7H	0.07	0.06	0.06	0.05	0.12	0.05	0.08	0.05	0.06	0.04
8H	0.08	0.06	0.06	0.05	0.13	0.06	0.08	0.05	0.06	0.05
9H	0.08	0.06	0.06	0.05		0.06		0.04		0.05
10H	0.08	0.06	0.06	0.05		0.06		0.06		0.05
11H	0.08	0.06	0.06	0.06		0.06		0.06		0.06
12H	0.08	0.06	0.07	0.06		0.07		0.06		0.06
13H		0.06	0.07	0.06		0.07				0.06
14H		0.07	0.07	0.06		0.07				0.06
15H		0.06	0.07							
16H			0.07							
17H			0.07							

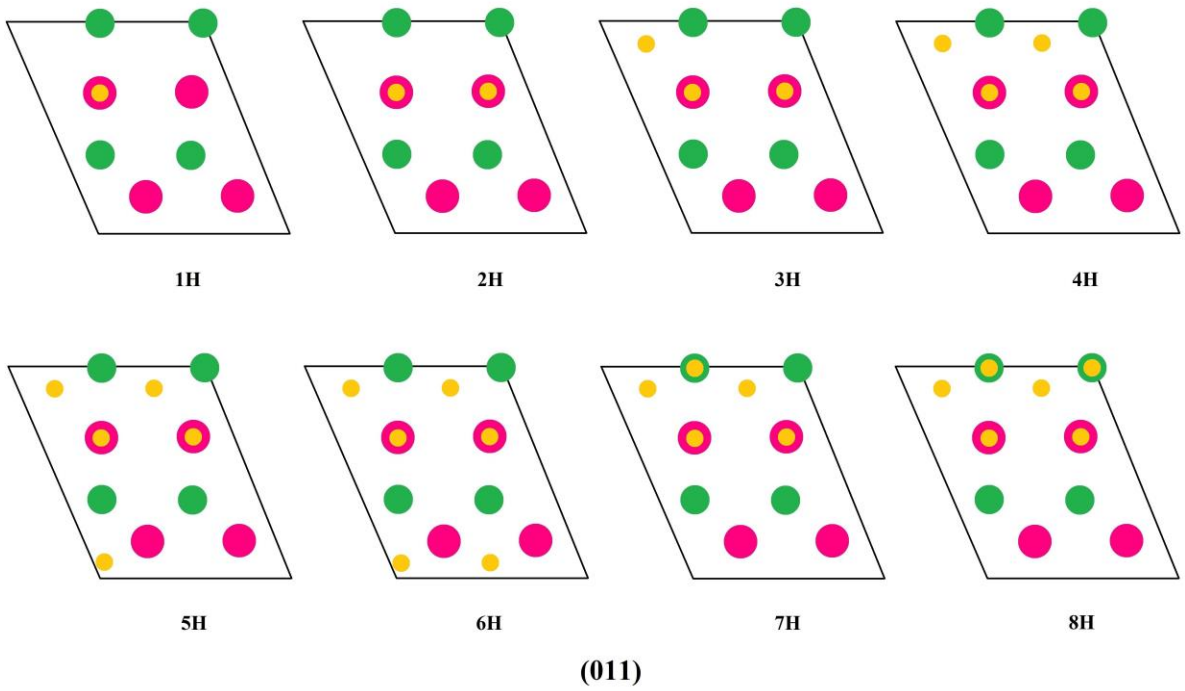

Figure 12. The hydrogen adsorption sites of (011) surface from low to high H coverage. The dark green circles are surface Mo atoms, and the dark magenta circles are surface C atoms. The hydrogen atoms are shown as the small yellow circles.

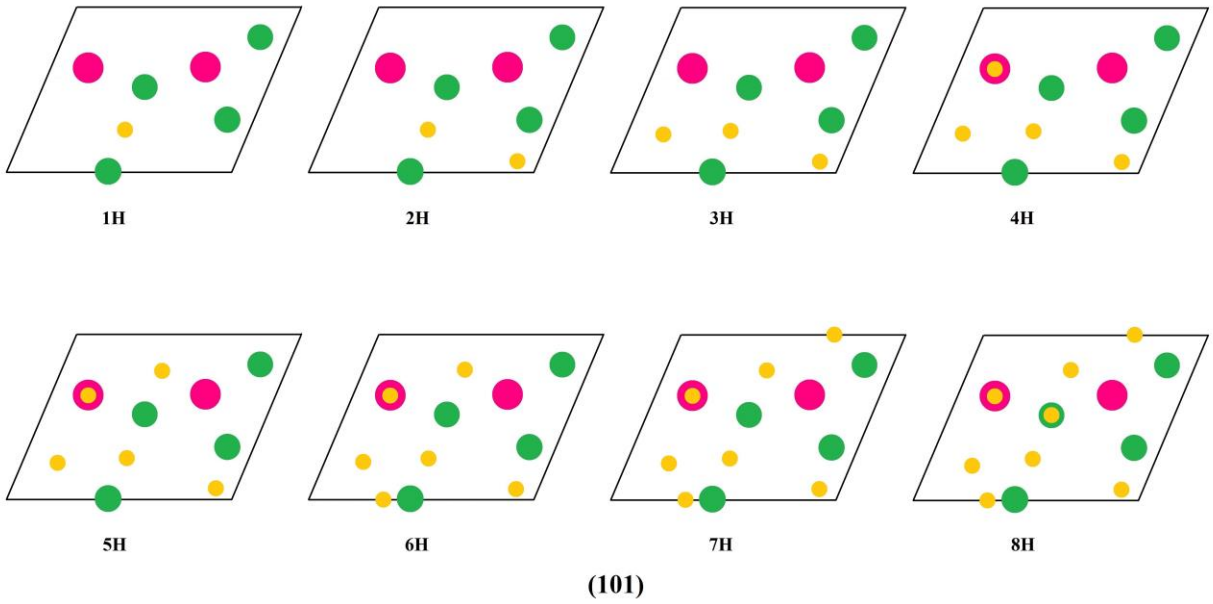

Figure 13. The hydrogen adsorption sites of (101) surface from low to high H coverage.

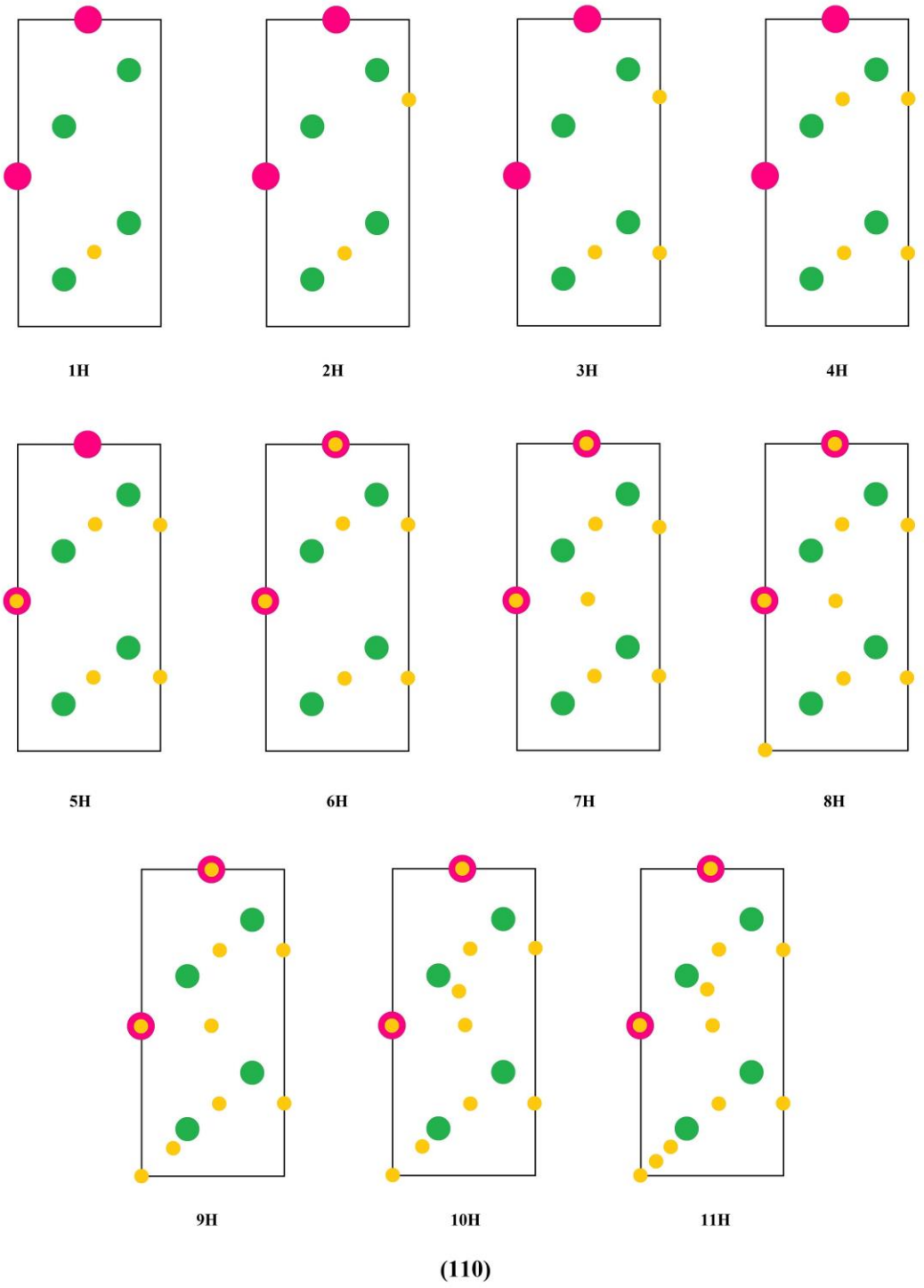

Figure 14. The hydrogen adsorption sites of (101) surface from low to high H coverage. As in (011) surface, hydrogen atoms occupy two identical sites with the same atomic coordination consecutively. For example, at 1H coverage, the adsorption site is at the bridge site of two Mo atoms on the 'bottom' of the supercell. At the next H coverage, hydrogen occupies the other bridge site on the 'top' of the supercell. At 7H and 8H coverage, the newly occupied hydrogen adsorption sites lie parallel to the surface atoms. At 11H coverage, the newly added hydrogen form hydroge dimer with the hydrogen added at 9H adsorption site.

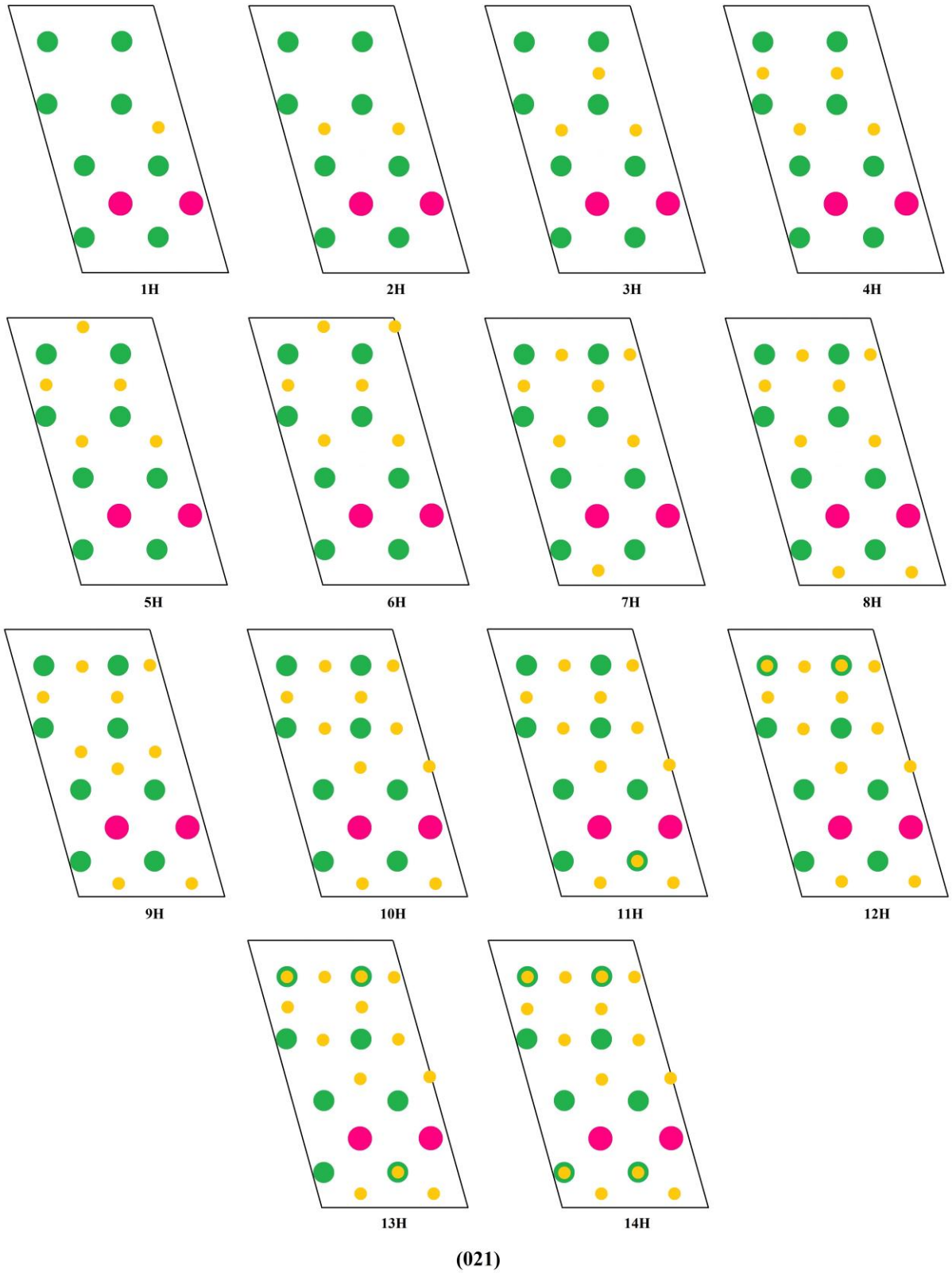

Figure 15. The hydrogen adsorption sites of (021) surface from low to high H coverage.

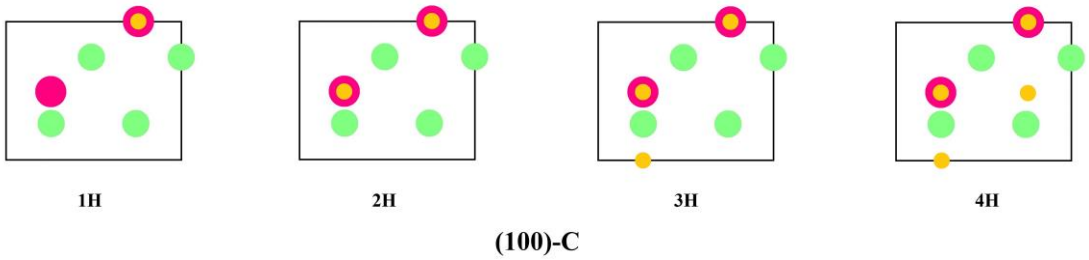

Figure 16. The hydrogen adsorption sites of (100)-C surface from low to high H coverage.

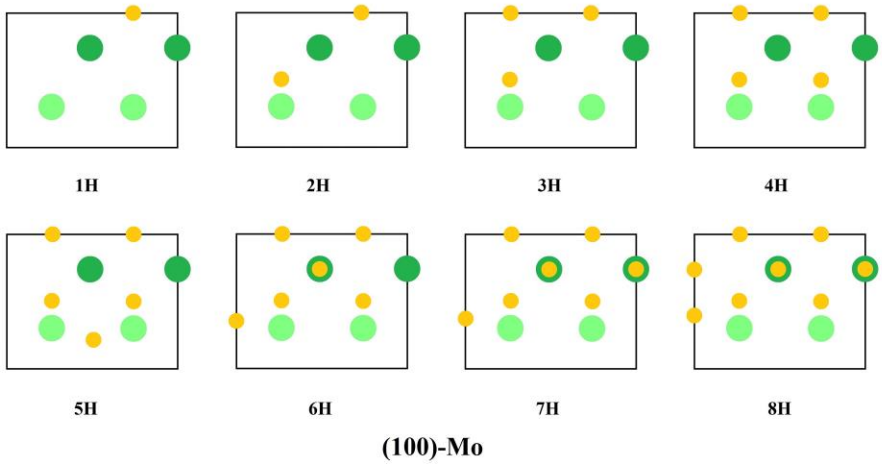

Figure 17. The hydrogen adsorption sites of (100)-Mo surface from low to high H coverage.

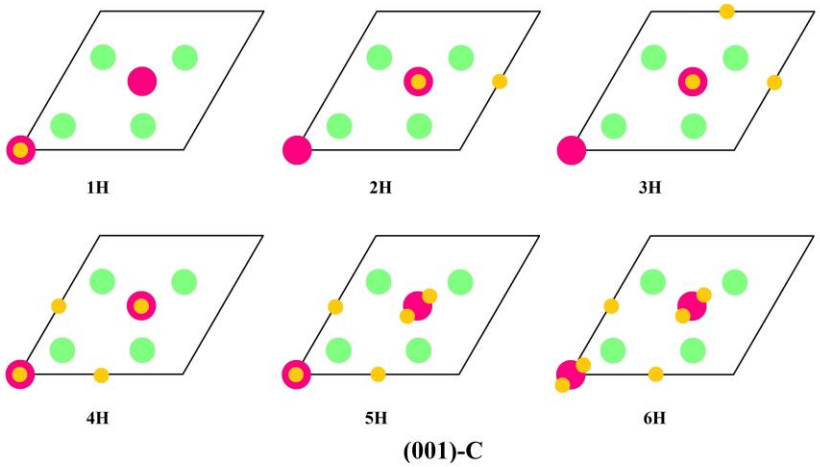

Figure 18. The hydrogen adsorption sites of (001)-C surface from low to high H coverage.

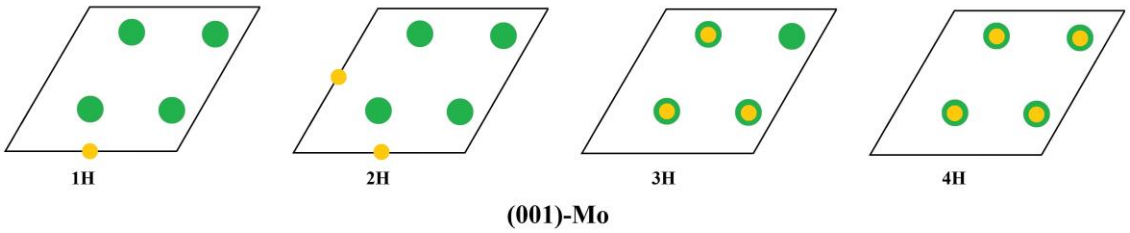

Figure 19. The hydrogen adsorption sites of (001)-Mo surface from low to high H coverage.

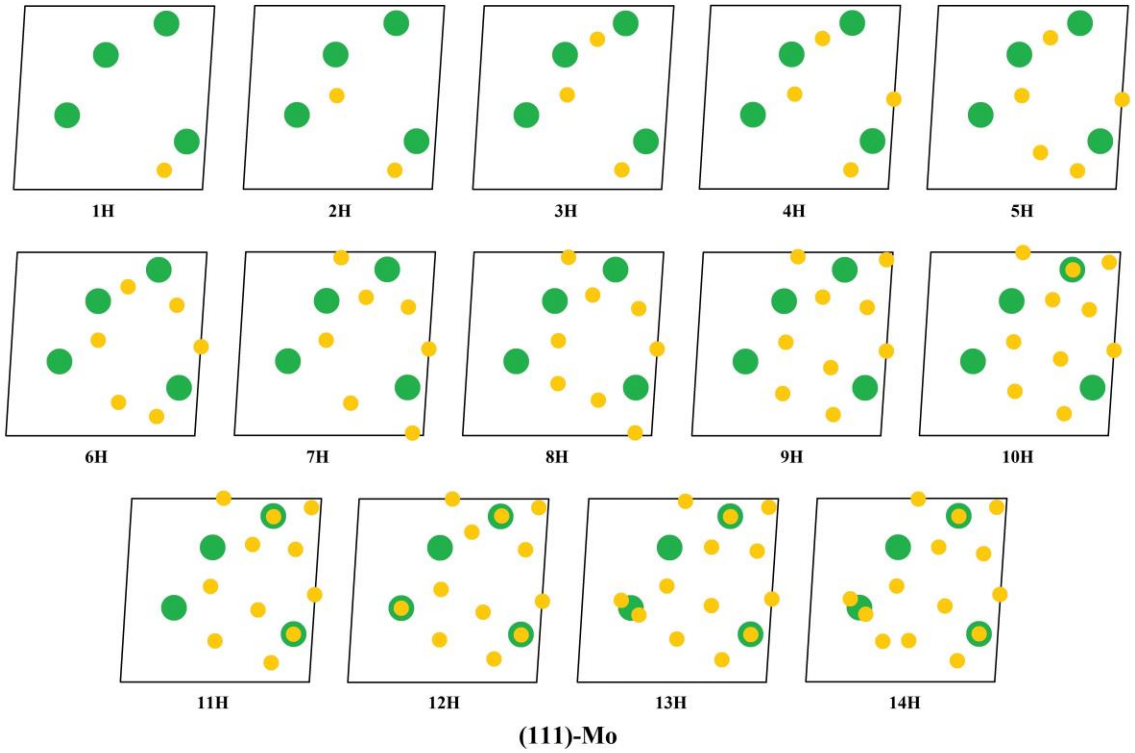

Figure 20. The hydrogen adsorption sites of (111)-Mo surface from low to high H coverage.

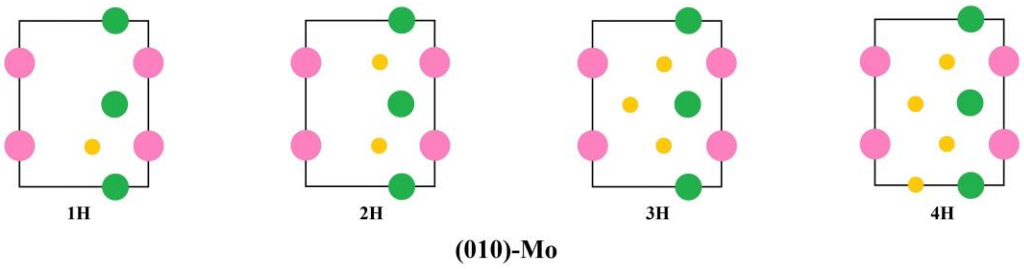

Figure 21. The hydrogen adsorption sites of (010)-Mo surface from low to high H coverage.

4.2 POTENTIAL ENERGY SURFACE

The optimum adsorption configurations can be largely understood by inspecting the potential energy surface (PES) of a single hydrogen atom on each surface. Based on the surface topology of different terminations, we identify six main adsorption sites: C top (C), Mo top (M), Mo bridge (B), Mo off-bridge (OB) and Mo hollow (H), as well as embedded (E) adsorption sites. The M/C top sites encompass hydrogen adsorption directly on top of the surface atom or in a tilted configuration with respect to the surface normal. For B or OB sites, the adsorbed hydrogen is in between, or slightly off, two surface Mo atoms. For H sites, mostly favoured on polar surfaces, hydrogen is coordinated with three Mo atoms. For E sites, which are high symmetry sites with respect to the sub-surface layer, hydrogen is nearly embedded flat on the surface. The adsorption energy of hydrogen at these sites are summarized in **Figure 22** and **Table 6**.

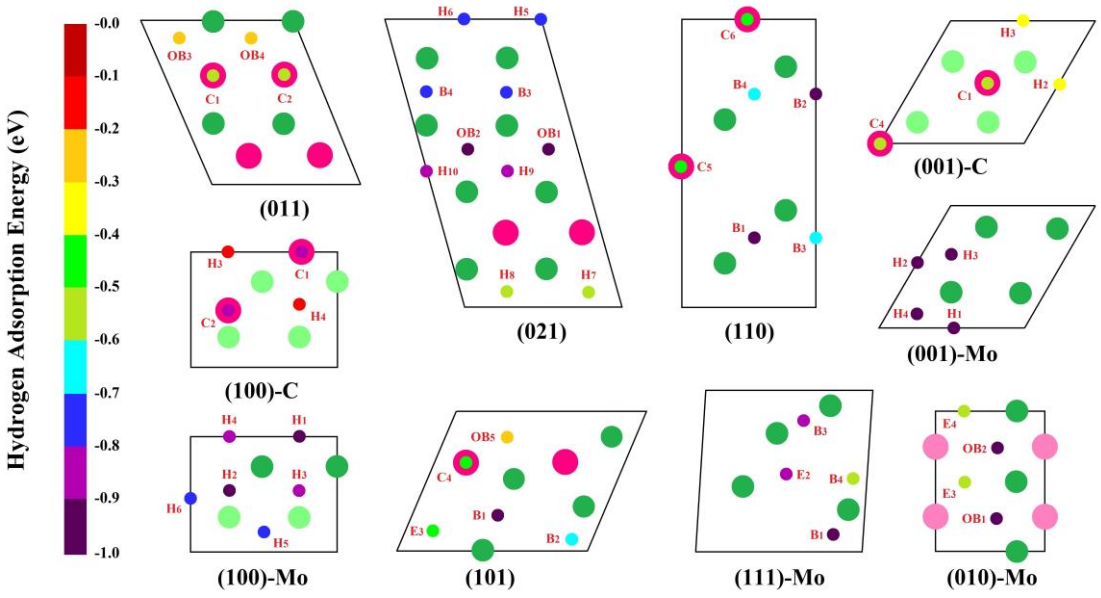

Figure 22. The adsorption sites (type shown in red) for ten studied surfaces as described in the text.

These optimum hydrogen adsorption configurations on β-Mo_2C are mainly dictated by the interactions of adsorbed hydrogen with surface Mo/C atoms as well as the interactions among hydrogen adsorbates. For most surfaces at low coverages, usually less than 6H, hydrogen interactions with surface atoms dictate the adsorption-site preferences, which can be understood from PES showed in **Figure 22**. This figure is constructed by placing a single hydrogen atom at each possible adsorption site. The subscripts indicate the hydrogen coverage at which the new site is occupied. For example, on (011), at 3H coverage, the third hydrogen occupies OB_3 site in the configuration at which C_1 and C_2 are occupied. The dark/light green circles are surface/sub-surface Mo atoms, and the dark/light magenta circles are surface/sub-surface C atoms. The strength of binding energies is color coded and shown as the small circles.

Table 6. DFT averaged hydrogen adsorption energy of hydrogen at adsorption sites on ten studied surfaces.

(011)		(101)		(110)		(021)		(111)-Mo	
C_1	-0.51	B_1	-0.95	B_1	-0.99	OB_1/OB_2	-0.94	B_1	-0.95
C_2	-0.51	B_2	-0.63	B_2	-0.99	H_9/H_{10}	-0.86	B_3	-0.87
OB_3	-0.21	E_3	-0.49	B_3	-0.66	B_3/B_4	-0.78	E_2	-0.85
OB_4	-0.21	C_4	-0.48	B_4	-0.66	B_5/B_6	-0.76	E_7	-0.74
		OB_5	-0.24	C_5	-0.41	H_7/H_8	-0.58	E_8	-0.66
				C_6	-0.41			B_4	-0.59

(100)-C		(100)-Mo		(001)-C		(001)-Mo		(010)-Mo	
C_1	-0.89	H_1	-0.93	C_1	-0.51	H_1	-1.06	OB_1	-0.94
C_2	-0.89	H_2	-0.93	C_4	-0.51	H_2	-1.06	OB_2	-0.94
H_3	-0.16	H_3	-0.89	H_2	-0.38	H_3	-0.97	E_3	-0.52
H_4	-0.16	H_4	-0.89	H_3	-0.38	H_4	-1.01	E_4	-0.52
		H_5	-0.79						
		H_6	-0.79						

The map shows that the adsorption sites are occupied in the sequence of decreasing *DFT averaged hydrogen adsorption energy* ΔE_{H^*}. Here (001)-Mo, (001)-C and (021) surface are exceptions because these surfaces have smooth PESs, as shown in **Table 6**. Noted that the we do not consider zero-point energy ΔE_{ZPE} for PES calculation because we show the ΔE_{ZPE} for each surface at each coverage are no more than 0.13 eV. More important, the ΔE_{ZPE} for each surface does not exceed 0.04 eV difference at the most and least vibrated coverage. Therefore, ΔE_{H^*} is accurate enough for describing the PESs.

4.3 BADER CHARGE ANALYSIS

In the previous section, we predict the hydrogen adsorption sites based on the potential energy surface. However, this simple picture, obtained from single-atom PES, fails to describe the optimum hydrogen adsorption configurations at high hydrogen coverages. As a result of the electrostatic interactions between adsorbed hydrogen atoms, which accept/donate charge upon adsorption, the interaction between the adsorbates and surface atoms significantly deform the potential surface. This is in line with the Helmholtz electrical double layer model that the there is a strong electric field in the heterogeneous interface. Indeed, Bader charge analysis in **Table 8** shows that ~0.3-0.4e charge is donated by Mo to hydrogen at Mo-related sites for all surfaces, but ~0.1-0.2e is donated from hydrogen to carbon for C site configurations.

Hydrogen adsorbates have a moderate interaction with surface at high coverage. In **Figure 23**, we show that the averaged Bader charge of hydrogen converges to 1 e (show as the dashed red line) as the *hydrogen adsorbed Gibbs energy* increases close to ΔG_{H^*} = 0. This explains that the electrons of surface atoms and hydrogen atoms almost stay in their orbitals

when hydrogen atoms are weakly adsorbed on the surface. Also, the neutral charge of hydrogen atoms confirms the formation of hydrogen molecules at $\Delta G_{H^*} \approx 0$.

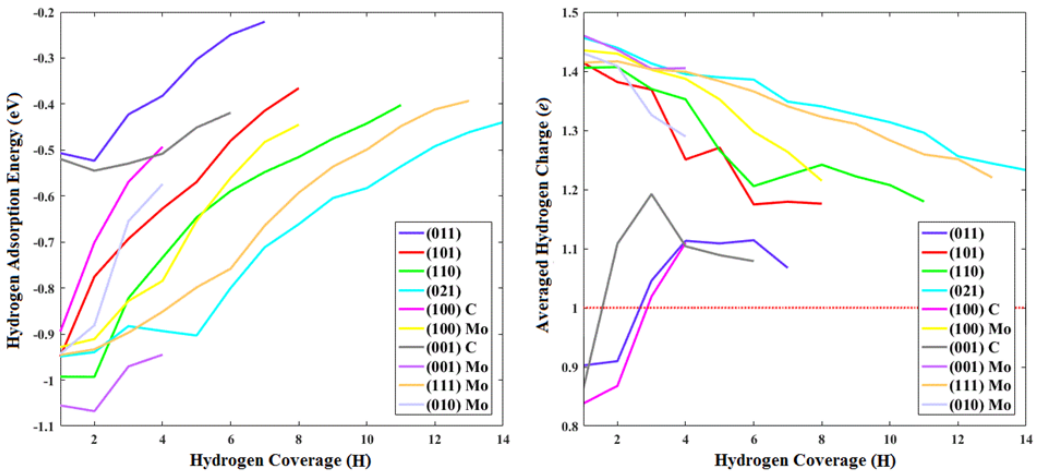

Figure 23. The adsorbed Gibbs free energy (left) and the averaged charge of an adsorbed hydrogen atom receives (right) with coverage dependence is calculated for ten surfaces.

Table 7. The *adsorbed Gibbs free energy* ΔG_{H^*} *(eV)* of the ten surfaces at *hydrogen coverage (H)*. We ignore the coverages that are less possible to appear on the system.

	(011)	(101)	(110)	(021)	(100)-C	(100)-Mo	(001)-C	(001)-Mo	(010)-Mo	(111)-Mo
1H	-0.51	-0.95	-0.99	-0.95	-0.89	-0.93	-0.52	-1.06	-0.94	-0.95
2H	-0.52	-0.78	-0.99	-0.94	-0.70	-0.91	-0.55	-1.07	-0.88	-0.93
3H	-0.42	-0.69	-0.82	-0.88	-0.57	-0.83	-0.53	-0.97	-0.65	-0.90
4H	-0.38	-0.63	-0.73	-0.89	-0.49	-0.78	-0.51	-0.95	-0.57	-0.85
5H	-0.30	-0.57	-0.65	-0.90		-0.65	-0.45			-0.80
6H	-0.25	-0.48	-0.59	-0.80		-0.56	-0.42			-0.76
7H	-0.22	-0.41	-0.55	-0.71		-0.48				-0.66
8H		-0.37	-0.52	-0.66		-0.44				-0.59
9H			-0.48	-0.60						-0.54
10H			-0.44	-0.58						-0.50
11H			-0.40	-0.54						-0.45
12H				-0.49						-0.41
13H				-0.46						-0.39
14H				-0.44						

Table 8. Bader charge analysis of adsorbed hydrogen on ten surfaces.

(011)		(101)		(110)		(021)		(111)-Mo	
C_1	0.90	B_1	1.41	B_1	1.41	OB_1/OB_2	1.46	B_1	1.41
C_2	0.90	B_2	1.36	B_2	1.41	H_9/H_{10}	1.44	B_3	1.43
OB_3	1.30	E_3	1.37	B_3	1.40	B_3/B_4	1.41	E_2	1.41
OB_4	1.30	C_4	0.90	B_4	1.40	B_5/B_6	1.41	E_7	1.42
		OB_5	1.32	C_5	0.95	H_7/H_8	1.41	E_8	1.40
				C_6	0.95			B_4	1.40

(100)-C		(100)-Mo		(001)-C		(001)-Mo		(010)-Mo	
C_1	0.84	H_1	1.44	C_1	0.87	H_1	1.46	OB_1	1.43
C_2	0.84	H_2	1.44	C_4	0.87	H_2	1.46	OB_2	1.43
H_3	1.25	H_3	1.44	H_2	1.34	H_3	1.43	E_3	1.33
H_4	1.25	H_4	1.44	H_3	1.34	H_4	1.44	E_4	1.33
		H_5	1.39						
		H_6	1.39						

Table 9. The *averaged hydrogen charge (e)* of the ten surfaces at *hydrogen coverage (H)*. We ignore the hydrogen adsorption sites that are less stable.

	(011)	(101)	(110)	(021)	(100)-C	(100)-Mo	(001)-C	(001)-Mo	(111)-Mo	(010)-Mo
1H	0.90	1.41	1.41	1.46	0.84	1.44	0.86	1.46	1.41	1.43
2H	0.91	1.38	1.41	1.44	0.87	1.43	1.11	1.44	1.42	1.41
3H	1.05	1.37	1.37	1.41	1.02	1.40	1.19	1.40	1.40	1.33
4H	1.11	1.25	1.35	1.39	1.11	1.39	1.10	1.40	1.40	1.29
5H	1.11	1.27	1.27	1.39		1.35	1.09		1.38	
6H	1.11	1.17	1.21	1.39		1.30	1.08		1.37	
7H	1.07	1.18	1.22	1.35		1.26			1.34	
8H		1.18	1.24	1.34		1.21			1.32	
9H			1.22	1.33					1.31	
10H			1.21	1.31					1.28	
11H			1.18	1.30					1.26	
12H				1.26					1.25	
13H				1.24					1.22	
14H				1.23						

4.4 DENSITY OF STATES

Most adsorption configurations are based on the interactions between hydrogen and Mo, and less with carbon. Although the most stable configurations for some surfaces at 1H are at C sites, the occupation of Mo-related sites precedes the C sites at high coverage. This can be explained from orbital and atom-projected density of states (PDOS) analysis of all investigated surfaces showing that the frontier orbitals in β-Mo_2C are mainly due to *p*- and *d*-Mo bands but not *p*-C bands. Namely, we found that 5*d*-band center of the Mo PDOS is located ~1.5-1.8 eV below the Fermi energy, while those due to 2*s*- and 2*p*-band centers of C atoms are located deeply in the valence band < 5 eV below the Fermi energy. See **Figure 24**.

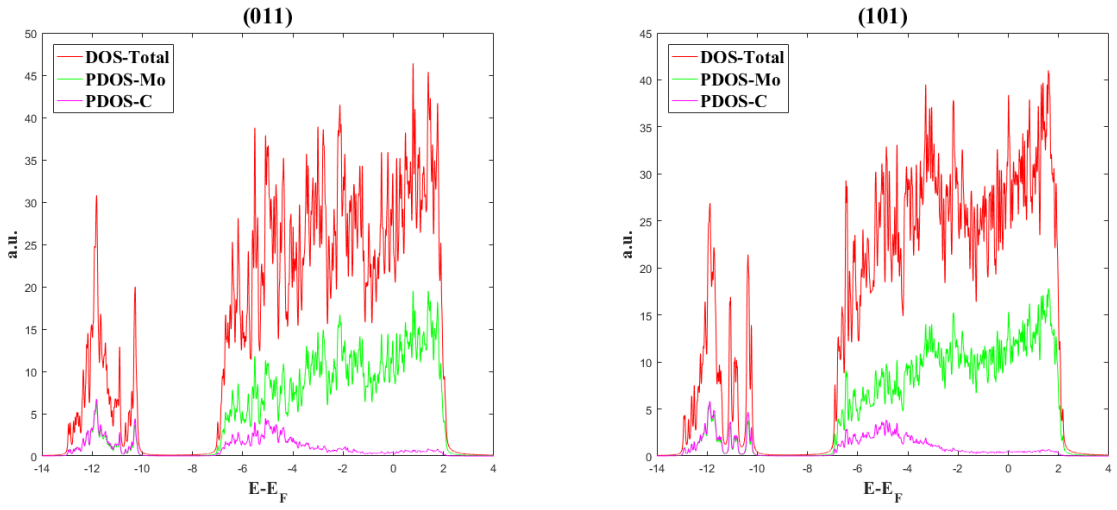

Figure 24. The density of states of the pristine ten β-Mo_2C surfaces.

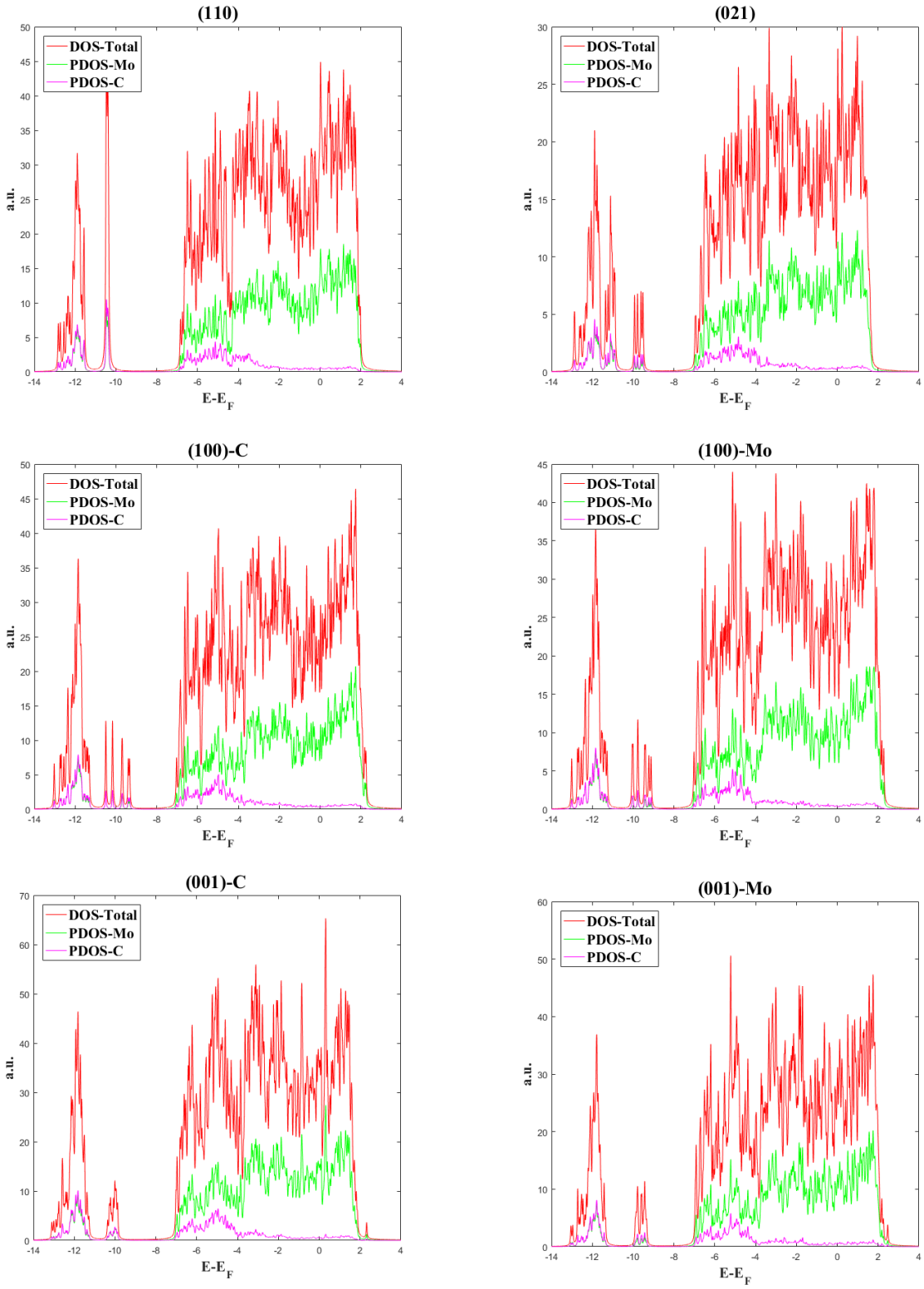

Figure 24 (continued). The density of states of the pristine ten β-Mo_2C surfaces.

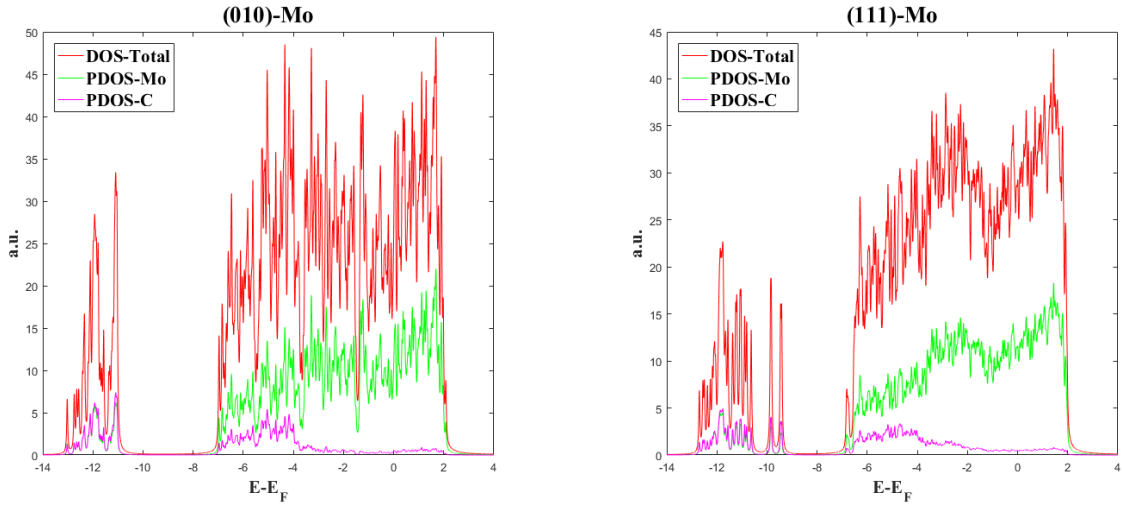

Figure 24 (continued). The density of states of the pristine ten β-Mo_2C surfaces.

4.5 AB INITIO THERMODYNAMIC ANALYSIS OF HYDROGEN ADSORPTION

In the previous sections, we determine the mechanism of hydrogen adsorption at zero temperature. The preferred hydrogen coverage corresponds to the case where the *total Gibbs free energy* is the lowest among all hydrogen coverages. However, at finite temperature, the hydrogen coverage on surface decreases with increasing temperature due to entropic reasons, which favor the gas phase, rather the adsorbed case. Therefore, for better correlation with experimental conditions during synthesis (typically 1000 K[31,34,65]) as well as HER measurements (typically at room temperature[66,67]), we compute the hydrogen composition phase diagrams **Figure 26** by inspecting the lowest total Gibbs free energy ΔG_{total} for different T and p values.

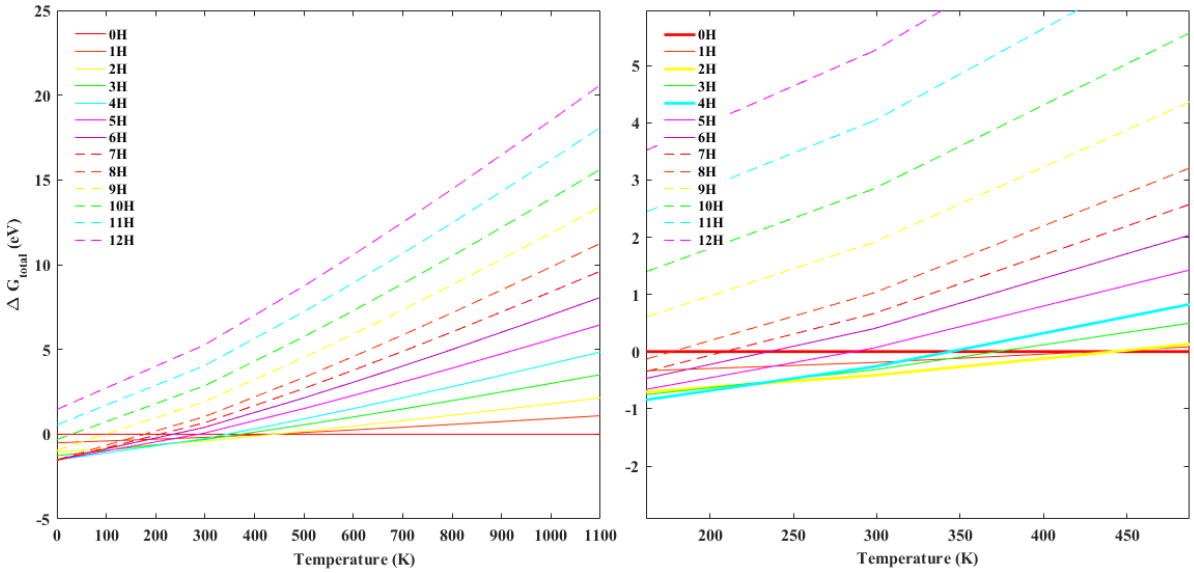

Figure 25. The *total hydrogen adsorption Gibbs free energy* ΔG_{total} of (011) surface from 0K to 1100K at 1 atm hydrogen partial pressure. The right picture is the zoomed in image of the left picture.

We take an example (011) surface at a 1 atm hydrogen partial pressure as shown in **Figure 25**. From 0 to 9 K, 9 K to 230K, 230 K to 440 K and beyond 440K, the system with the lowest ΔG_{total} is the most stable when the hydrogen coverage is 7H, 4H, 2H and 0H at these temperature values. The hydrogen composition phase diagrams are essential to predict the hydrogen coverages in hydrogen gas environment, *e.g.* for NPs Wulff construction at synthesis temperature and the exchange current densities at ambient temperature. Note that the hydrogen evolution reaction usually takes place in acidic or alkaline electrolyte such as 0.1 M $HClO_4$, 0.5M or 1M H_2SO_4, 1 M KOH with excess of water molecules. In our analysis, we exclude the interactions with water molecules to avoid high computational cost. In the future, we will extend our work to include the water environment as well as effect of external voltage.

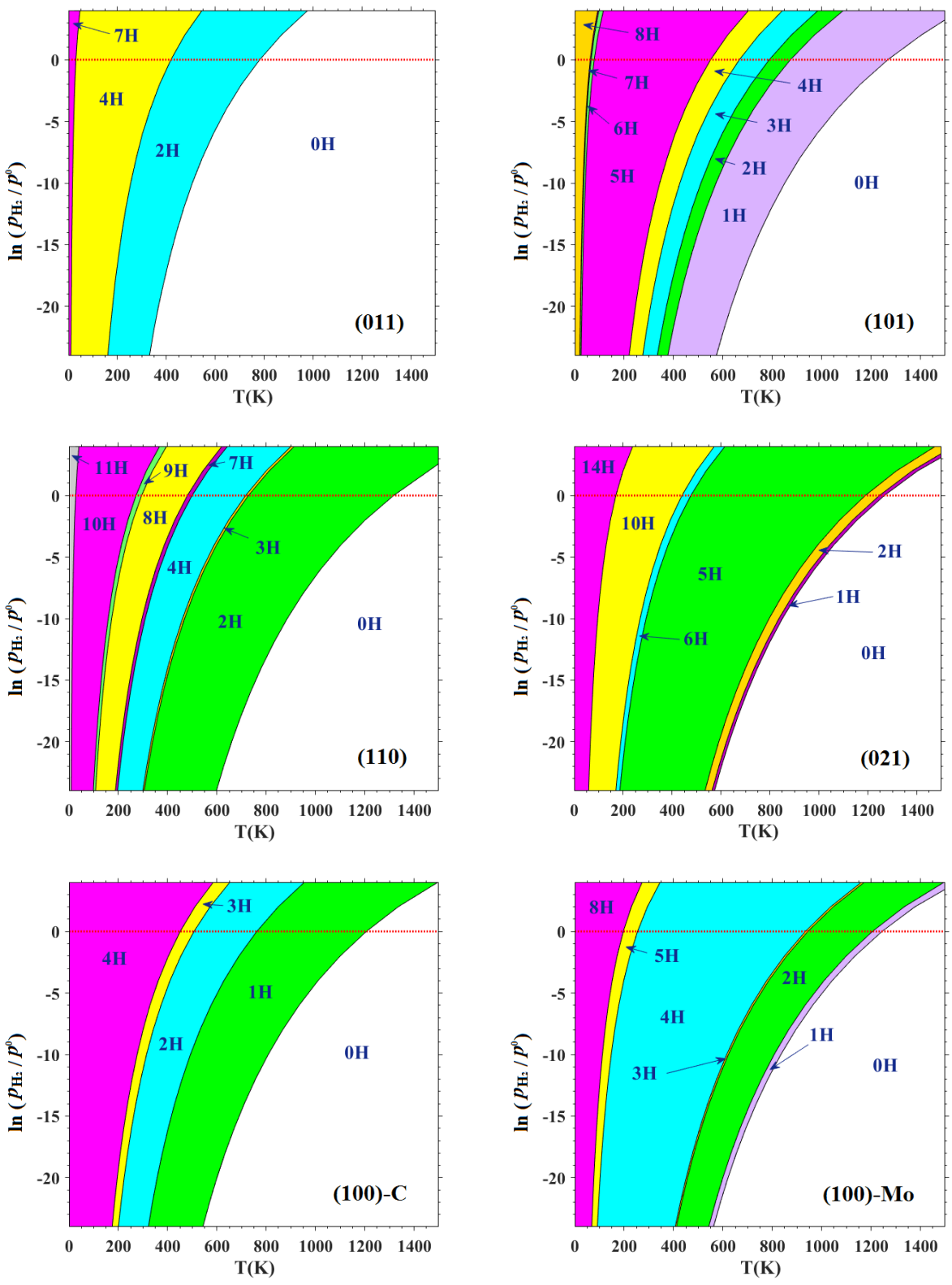

Figure 26. Hydrogen surface composition on ten surfaces as a function of temperature and pressure. The red line corresponds to the standard state pressure p^0 =1 atm.

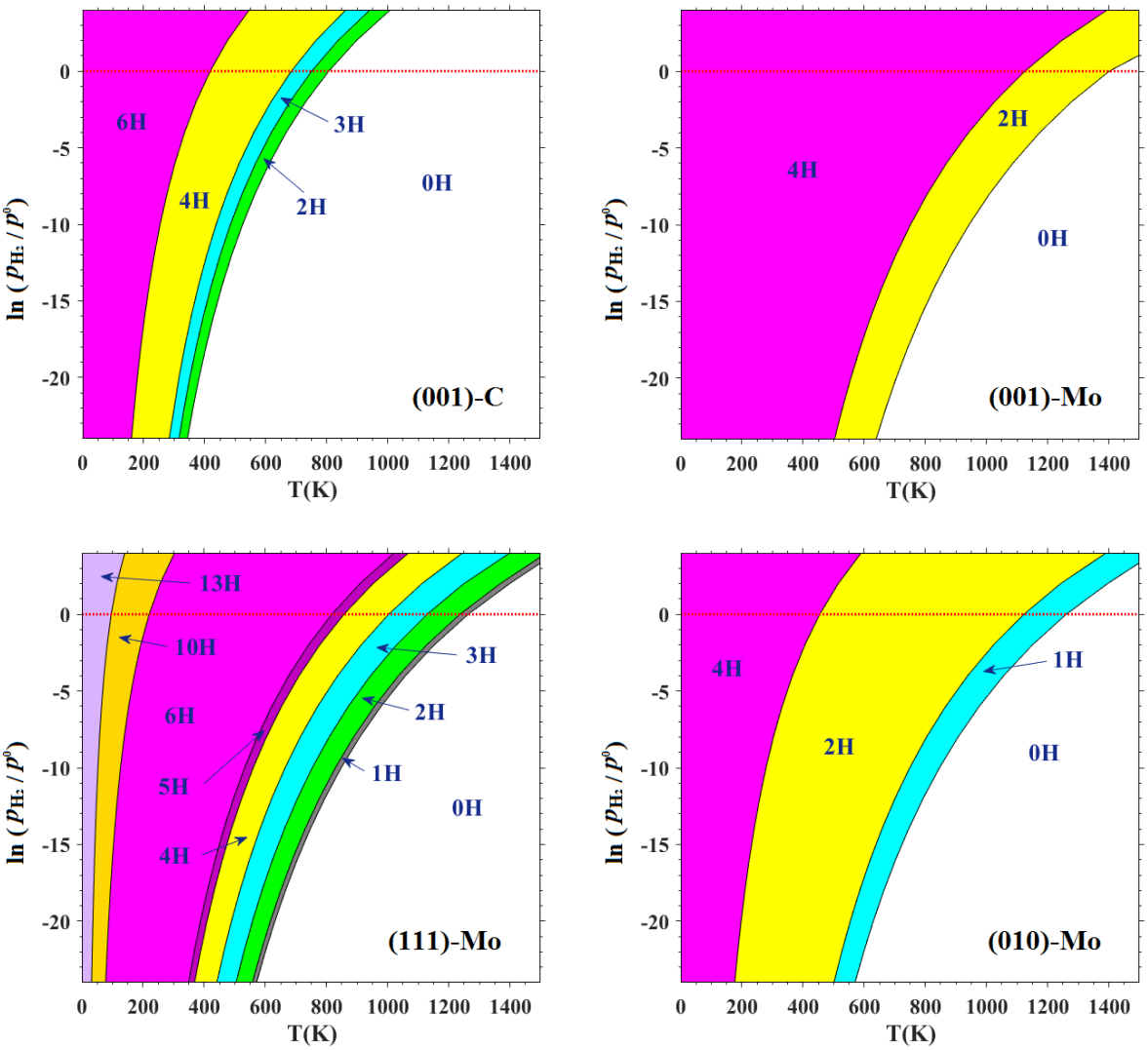

Figure 26 (continued). Hydrogen surface composition on ten surfaces as a function of temperature and pressure. The red line corresponds to the standard state pressure p^0 =1 atm.

5.0 THE FORMATION OF NANOPARTICLES

We investigate the hydrogen adsorption on β-Mo_2C surfaces and conclude the high hydrogen evolution reaction activity of (011) surface, as discussed in the previous chapter. In this chapter, we will discuss the surface stability of β-Mo_2C surfaces by inspecting the *surface free energy*, and the proportions of these surfaces that can be stabilized on β-Mo_2C nanoparticles, and how these varies by controlling carbon chemical potential and temperature. In addition, we study the hydrogen effect on the morphology of NPs to better understand the formation of these NPs under synthesis conditions at 1000 K.

5.1 SURFACE FREE ENERGY

The morphology of β-Mo2C NPs in thermodynamic equilibrium is determined by Wulff construction based on the prescription of minimizing surface free energy. We use non-stoichiometric surface models with equivalent surface terminations on both sides of the slabs, therefore, the β-Mo2C surface energy dependents on only one chemical potential. **Figure 27** shows that μ_C has a dramatic effect on surface stability, and consequently the morphology of NPs as we discuss later. Further, we include temperature effect arising from atomic vibrations, as these are important at synthesis temperatures (~1000 K).[31,34,65] In **Figure 27**, we compare the

surface free energy of the ten surfaces at 0 K (solid lines) and 1000 K (dashed lines) and the detailed values are showed in both of the **Table 10** and **Table 11**.

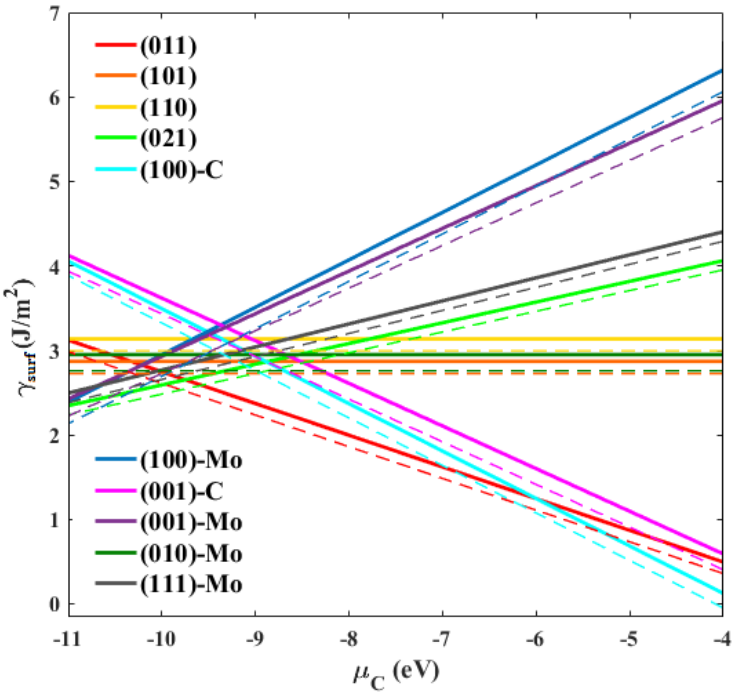

Figure 27. The surface free energy of the ten selected surfaces γ_{surf} at 0K (solid lines) and 1000K (dashed lines).

Table 10. The *surface free energy* of the ten surfaces at 0 K.

μ_c	(011)	(101)	(110)	(021)	(100)-C	(100)-Mo	(001)-C	(001)-Mo	(010)-Mo	(111)-Mo
-4	0.50	2.87	3.14	4.06	0.13	6.32	0.59	5.96	2.95	4.41
-5	0.87	2.87	3.14	3.82	0.69	5.76	1.10	5.45	2.95	4.13
-6	1.25	2.87	3.14	3.57	1.25	5.20	1.60	4.95	2.95	3.86
-7	1.62	2.87	3.14	3.33	1.81	4.64	2.11	4.45	2.95	3.59
-8	2.00	2.87	3.14	3.08	2.37	4.07	2.61	3.94	2.95	3.31
-9	2.37	2.87	3.14	2.84	2.93	3.51	3.12	3.44	2.95	3.04
-10	2.75	2.87	3.14	2.59	3.50	2.95	3.62	2.93	2.95	2.77
-11	3.12	2.87	3.14	2.35	4.06	2.39	4.12	2.43	2.95	2.50

Table 11. The *surface free energy* of the ten surfaces at 1000 K.

μ_C	(011)	(101)	(110)	(021)	(100)-C	(100)-Mo	(001)-C	(001)-Mo	(010)-Mo	(111)-Mo
-4	0.36	2.73	3.00	3.96	0.00	6.06	0.41	5.76	2.76	4.29
-5	0.74	2.73	3.00	3.71	0.52	5.50	0.91	5.25	2.76	4.02
-6	1.11	2.73	3.00	3.47	1.08	4.94	1.42	4.75	2.76	3.75
-7	1.49	2.73	3.00	3.22	1.64	4.38	1.92	4.24	2.76	3.48
-8	1.86	2.73	3.00	2.97	2.20	3.82	2.42	3.74	2.76	3.20
-9	2.24	2.73	3.00	2.73	2.76	3.26	2.93	3.23	2.76	2.93
-10	2.61	2.73	3.00	2.48	3.33	2.70	3.43	2.73	2.76	2.66
-11	2.99	2.73	3.00	2.24	3.89	2.13	3.94	2.23	2.76	2.39

5.2 SURFACE STABILITY IN HYDROGEN AMBIENT

The effect of the hydrogen ambient on the NP morphology can be determined from the hydrogen adsorption contribution to surface free energy, which can be read from **Figure 26**. The absolute value of hydrogen adsorbed surface free energy, $\gamma_{H_2}(T, p^{\circ})$, at several selected temperatures in 1 atm hydrogen partial pressure environment is shown in **Figure 27** and details in **Table 12**. As seen from the figure, $\gamma_{H_2}(T, p^{\circ})$ is relatively low at high temperatures and high at low temperatures. This is because that at low temperatures, hydrogen atoms are more likely to be stabilized on the surface by passivating dandling bonds.

On the other hand, hydrogen atoms are unlikely to be adsorbed on surface at high temperature due to entropic preference of the gas phase. Thus, we conclude that hydrogen ambient has no effect on surface energies, and consequently of the nanoparticles morphology at relevant synthesis temperatures. To investigate the morphology of nanoparticles synthesized at 600K, 800K and 1000K, we compute the surface free energy at these temperatures for the ten selected surfaces as shown in **Table 11** and **Table 12**, and further use these calculated surface

free energies with the hydrogen adsorption correction term to predict the shapes of these nanoparticles using Wulff's construction theory as we will discuss in the following section.

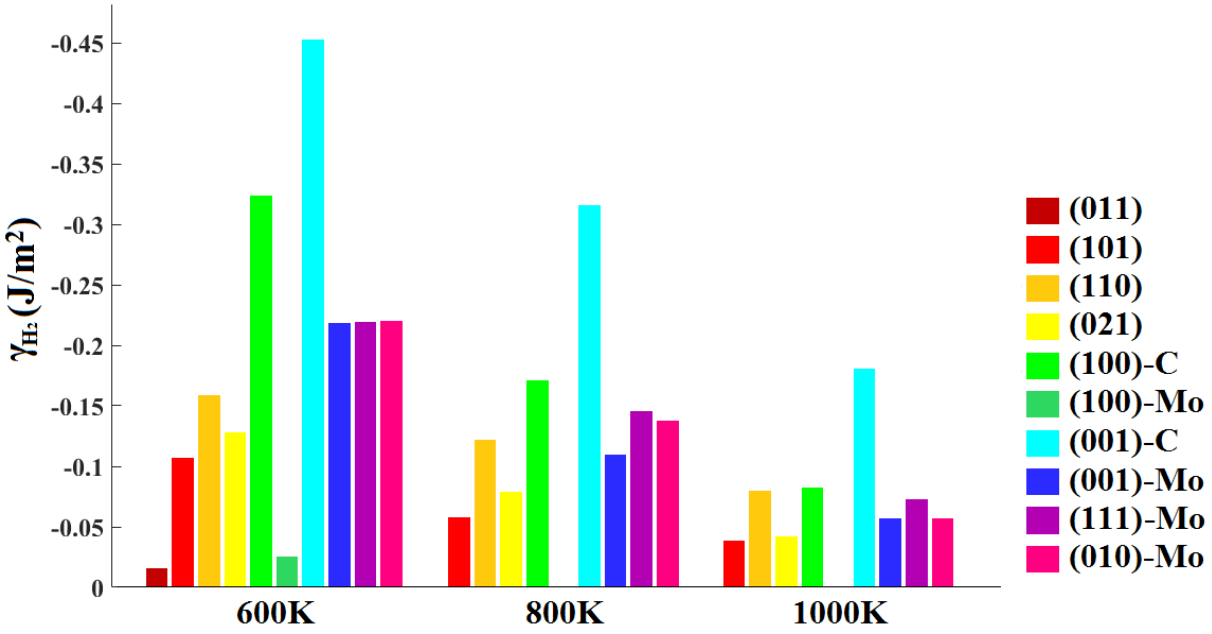

Figure 28. The hydrogen adsorbed surface free energy, $\gamma_{H_2}(T, p^{\circ})$, at three selected temperatures at 1 atm hydrogen partial pressure.

Table 12. The Surface free energy of the ten surface in 1 atm hydrogen partial pressure ambient at 600K, 800K and 1000K.

	(011)	(101)	(110)	(021)	(100)-C	(100)-Mo	(001)-C	(001)-Mo	(010)-Mo	(111)-Mo
600K	-0.02	-0.11	-0.16	-0.22	-0.13	-0.32	-0.03	-0.45	-0.22	-0.22
800K	0.00	-0.06	-0.12	-0.14	-0.08	-0.17	0.03	-0.32	-0.15	-0.11
1000K	0.00	-0.04	-0.08	-0.06	-0.04	-0.08	0.00	-0.18	-0.07	-0.06

5.3 THE MORPHOLOGY OF NANOPARTICLES

β-Mo_2C NPs can be synthesized via different methods. One of the traditional ways is through temperature-programmed reduction. Here the β-Mo_2C carburization process is conducted at atmospheric pressure using MoO_3 as precursor and CH_4/H_2, C_2H_6/H_2, C_3H_8/H_2, C_4H_{10}/H_2, or CO/H_2 gas mixture as carbon source, provided from the dissociation of these gas mixtures into carbon and hydrogen gas. The other common route to synthesize β-Mo_2C is through mixing $(NH_4)_6Mo_7O_24(H_2O)$ and sucrose[68], glucose[69] or 4-Cl-o-phenylenediamine[36] in water to form decomposition products MoO_3 and C. Then, Mo_2C NPs are formed through chemical reaction[68] $2MoO_3+7C \rightharpoonup Mo_2C+6CO$ in a tube furnace under argon[36,69], hydrogen[69] or nitrogen[70] gas at about 1000K. From these two synthesis routes, we can see that the solid phase carbon plays a key role to potentially affect NP morphology, and it is certainly involved in every β-Mo_2C synthesis approach. In addition, the presence of ambient $H_2(g)$ in some synthesis processes may also play a role in NP morphology. In this study, we focus on β-Mo_2C synthesis conditions that take place at elevated temperature T ~1000K, at which the growth and morphology of the NPs are dictated by thermodynamic factors, namely changes in surface free-energy due to carbon chemical potential or hydrogen adsorption, rather than kinetic factors that result in shape-selective growth[71-75].

We first discuss the effect of variations in the carbon chemical potential. Based on the surface energies at T=1000K with zero hydrogen partial pressure, and using the experimentally resolved P63/mmc space group of β-Mo_2C [31,36,47,76], we determine the morphology of β-Mo_2C NPs using Wulff construction[77], as shown in **Figure 29**. The Wulff construction provides a recipe to determine the equilibrium shape of the NPs at fixed volume by minimizing its surface energy. As anticipated from the surface energies in **Figure 27**, we see that the carbon chemical

potential has a dramatic effect on the morphology. For instance, the exposed percentage of the most HER active (011) surface increases through 61.9%, 74.9%, 83.1% and 88.0% as the carbon chemical potential decreases from -6 to -9 eV. At $\mu_C = -10\ eV$, the NPs start to expose (021) surface. Previously, Wang and collaborators determined the morphology of Wulff constructed β-Mo_2C NPs using a similar approach to that employed in our study except that they included a larger subset of non-stoichiometric surface terminations. In their study, they considered synthesis conditions with partial pressure ratio of CH_4: H_2 = 1:4 atm, which corresponds to $\mu_C \sim -9.5$ eV. They showed that the NPs at 1000 K exposes 83% of (011) followed by 13% of (001)[43]. (Note that the (101) in Ref. 43 is equivalent to (011) in our work). This result is in very good agreement with the NPs obtained in our study at the chemical potential of -8 and -9 eV, which corroborates that selection of low energy surfaces is relevant to the study of NP morphology.

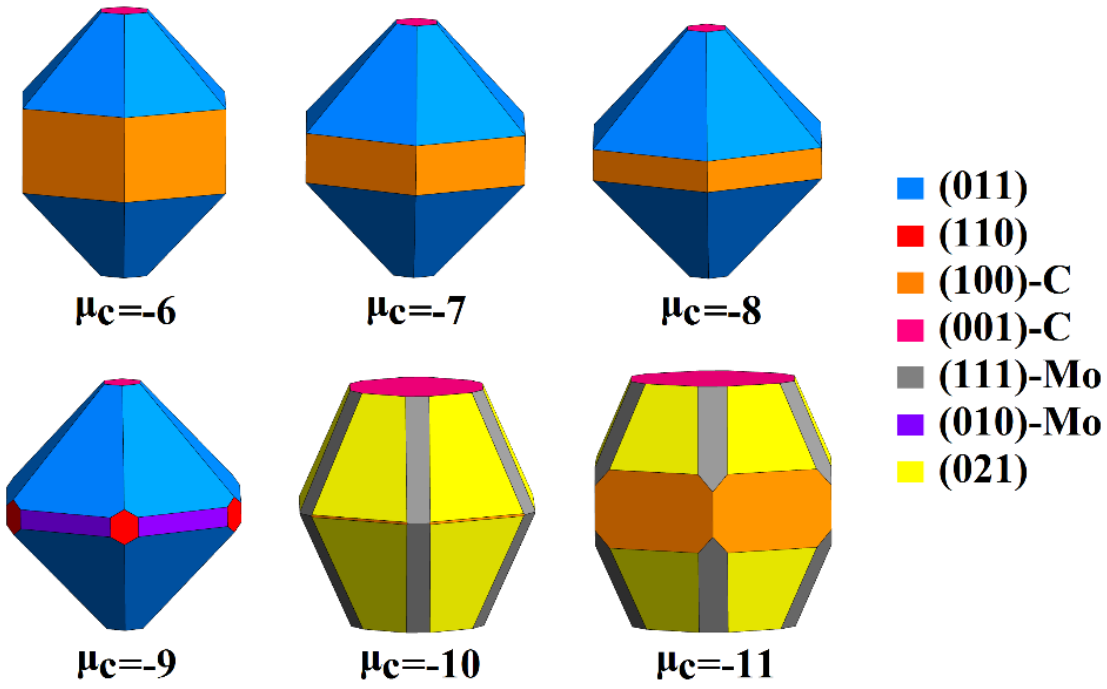

Figure 29. Evolution of β-Mo2C NPs at various carbon chemical potentials.

We also study the hydrogen effect on the morphology of NPs based on the surface free energy which are discussed in the previous section. At low temperature 600 K where γ_{H_2} is more than half of the absolute values at 1000 K, the morphology of nanoparticles show a distinguishable change of the surface composition.

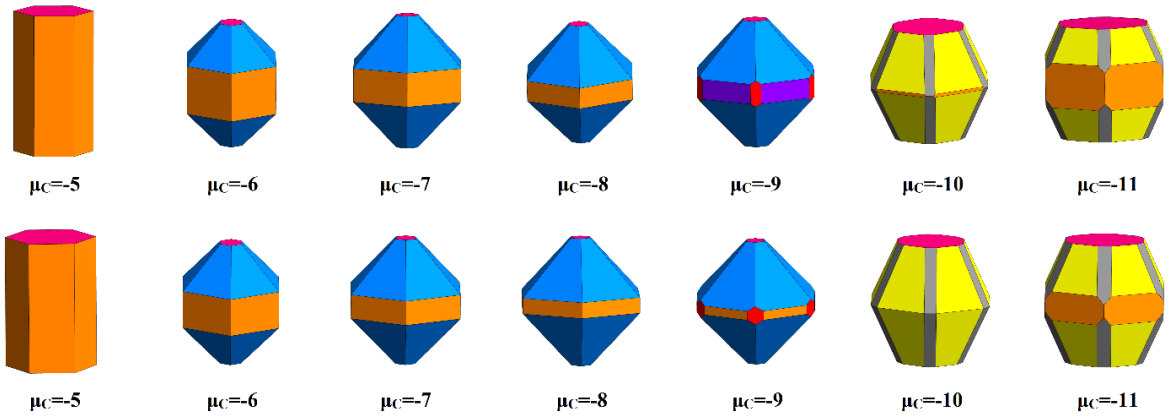

Figure 30. Nanoparticles synthesized at 600 K. The first row are the NPs synthesized at hydrogen partial pressure at 1 atm. The first row shows the NPs synthesized at hydrogen partial pressure of 0 atm.

In, **Figure 30**, we compare the NPs synthesized at 600 K with 1 (first row) and 0 atm (second row) hydrogen partial pressure. At both hydrogen partial pressures, NPs at the same chemical potential range expose the same terminations except that their proportions are different: At $\mu_C = 5$ eV, two surfaces are exposed on the NPs, namely the orange (001)-C surface and magenta (100)-C. For μ_C in the range of -6 eV and -9 eV, the three surfaces of (100)-C, (001)-C and (011) are exposed. For μ_C is less than -10 eV, the four exposed surfaces are (001)-C, (021), (111)-Mo and (100)-C. Comparing the NPs at 0 atm and 1 atm hydrogen partial pressure, a larger percentage of (011) surface is exposed in the chemical potential range from μ_C=-6 and $\mu_C = -9$ eV. However, at elevated temperature 1000 K, the role of hydrogen partial pressure cannot be

discerned as shown in **Figure 31**. This is because that the hydrogen atoms cannot be stabilized on surface with a high thermal energy contribution, so that there are only a small interaction between surface and hydrogen with the hydrogen ambient at 1000 K.

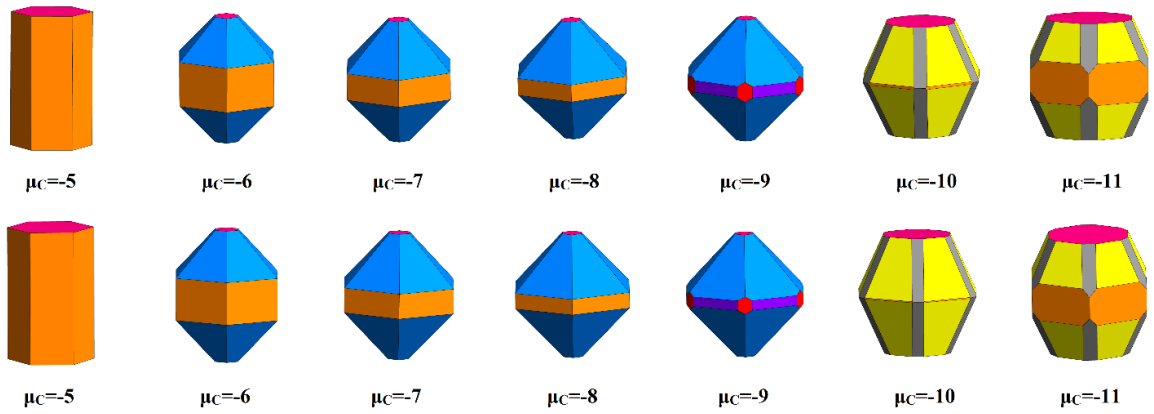

Figure 31. Same as the previous figure, but for nanoparticles synthesized at 1000 K.

6.0 THE EXCHANGE CURRENT DENSITY ON NANOPARTICLES

In the previous chapter, we predict the morphology of β-Mo_2C Nanoparticles, and show that the catalytic (011) surface can be largely exposed on NPs at a range of carbon chemical potential between -6 and -9 eV. In this chapter, we will use a simple kinetic model of exchange current density to link the HER activity of β-Mo_2C structures with experiments. We will show that the HER efficiency of the optimized β-Mo_2C nanoparticle is comparable to that of platinum, which is the most efficient HER catalyst.

6.1 THE DEFINITION OF EXCHANGE CURRENT DENSITY

Current is generated when electrons are discharged from adsorbed hydrogen during HER reaction. At equilibrium, the forward r_F and backward r_B reaction rates are equal and these can be related to proton concentration C_{H^+} on the electrode according to total reaction of HER[78],

$$r_F = k_f\,(1-\theta)\,C_{H^+}$$

$$r_B = k_b\,(\theta)\,C_{H^+}.$$

These equations can be used to define the hydrogen converge θ as,

$$\theta = \frac{k_f/k_b}{1+k_f/k_b} = \frac{K_{eq}}{1+K_{eq}},$$

where $K_{eq} = k_f/k_b = e^{-\Delta G_{H^*}/k_\beta T}$ is related to the hydrogen adsorption energy. The exchange current can be readily expressed from the reaction rates, as

$$i_0 = -er_0 = -er_F = -er_B$$

where e is the electron charge (positive). For exothermic process of proton transfer ($\Delta G_{H^*} < 0$), the exchange current is determined by forward rate,

$$i_0 = -er_0 = -er_f = -ek_0 \frac{1}{1 + e^{-\Delta G_H/k_\beta T}}$$

On the other hand, if proton transfer is endothermic ($\Delta G_{H^*} > 0$), then the backward rate is used to compute the exchange current

$$i_0 = -er_0 = -er_b = -ek_0 \frac{e^{-\Delta G_{H^*}/k_\beta T}}{1 + e^{-\Delta G_{H^*}/k_\beta T}}$$

Current is generated when electrons are discharged from adsorbed hydrogen during HER reaction. For exothermic proton-transfer process ($\Delta G_{H^*} < 0$), as is the case for β-Mo_2C NPs, the exchange current density is

$$j_0 = -\frac{ek_0}{A} \frac{1}{1 + e^{-\frac{\Delta G_{H^*}}{k_\beta T}}}$$

where k_0 is the rate constant and A is the electrode surface area. For a NP, we assume that the exchange current density J_0 is the sum of $j_0^{(i)}$s from each distinct surface

$$J_0 = \sum_i j_0^{(i)} = -ek_0 \sum_i A_i \rho_i \frac{1}{1 + e^{-\frac{\Delta G_{H_i^*}}{k_\beta T}}}$$

Here A_i is area percentage of ith surface in the NP, and $\boldsymbol{\rho_i}$ is the density of active sites, which is the hydrogen coverage per unit surface area for each termination. We assume that all β-Mo_2C surfaces have the same k_0 value, which is in line with previous assumption of using the same rate constant value for all metals[79].

The exchange current density j_0, the exchange current per unit area of electrode, is experimentally the most general way to describe HER activity. Examining hydrogen adsorption Gibbs free energy ΔG_H^* vs. j_0 on metal surfaces[79], it was shown their correlation results in volcano plot when plotting ΔG_H^* along *x*-axis and j_0 along *y*-axis. The peak of the volcano corresponds to the maximum value of j_0 with respect to $\Delta G_H^*=0$, and it separates the two symmetric tails; the left tail with $\Delta G_H^* < 0$ is where the j_0 is generated by exothermic process of proton transfer, and the right tail with $\Delta G_H^* > 0$ is for endothermic process. For a good HER catalyst, hydrogen adsorption energy satisfies $\Delta G_H^* \simeq 0$, i.e. hydrogen binding to the surface is neither too strong nor too weak.

6.2 THE CALCULATION OF EXCHANGE CURRENT DENSITY

To compute the HER activities of the β-Mo_2C surfaces and NPs by exchange current densities, we first estimate the rate constant k_0 by utilizing the experimentally measured current densities. For consistency, we selected all reported exchange current density values from β-Mo_2C NPs synthesized through the same acidic solution route by using ammonium molybdate as precursor[36,47,69,80-82]. Under such synthesis condition, the terminations of (011), (100), (001) and (111) are reported from transmission electron microscopy (TEM) measurements.[80,47,68,69,81] These results are consistent with the morphologies predicted at μ_C = -6, -7, -8, and −9 eV. In conjunction with the density of active sites ρ_i for each surface at experimental HER conditions, we estimate that k_0 ranges from 1.8×10^{17} to 2.5×10^{18} $s^{-1}cm^{-2}$, and this range reflects the variation in the experimental measurements. For comparison, the value of k_0 reported for metallic surfaces is 3.0×10^{17} $s^{-1}cm^{-2}$.[79] Using ΔG_{H^*} for each surface at the equilibrium hydrogen coverage at 298K

obtained from **Figure 26**. we calculate the exchange current densities of the ten terminations and the net exchange current of the predicted β-Mo_2C nanoparticles synthesized from different carbon chemical potentials. Our results for the β-Mo_2C surfaces and NPs can be all described using the volcano curve predicted from metal surfaces[79], as seen in **Figure 32**.

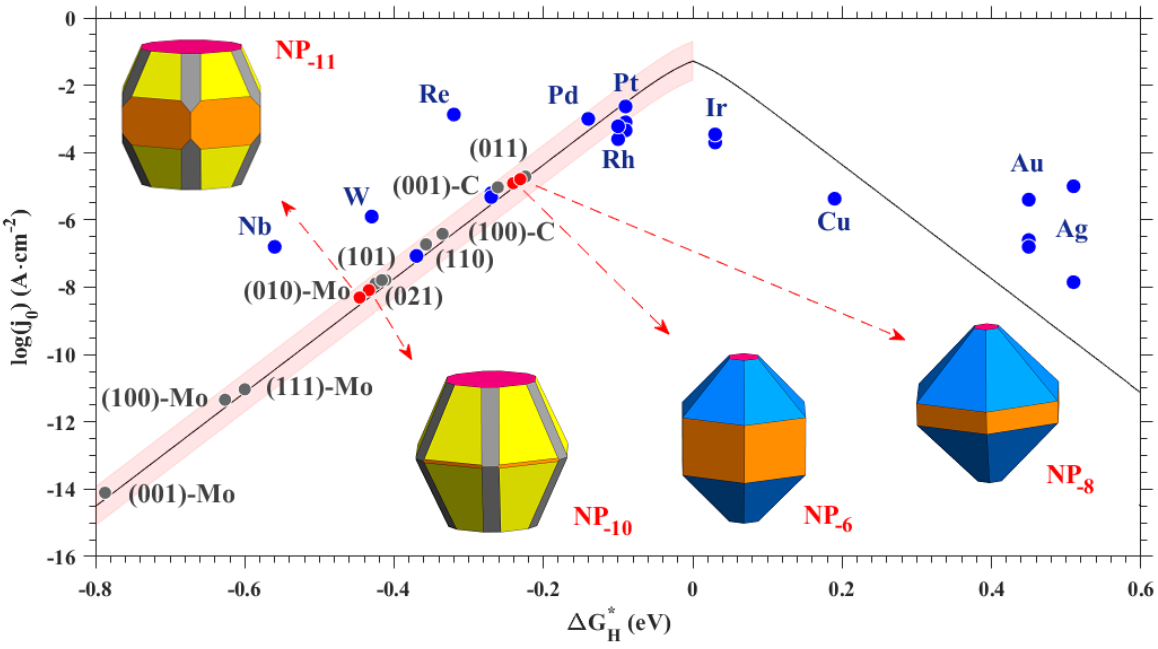

Figure 32. The exchange current densities as a function of hydrogen adsorbed free-energy are shown for metal surfaces[79], DFT predicted nanoparticles and surface terminations. The black curve is plotted by selecting $k_0 = 8\times10^{17}\mathrm{cm}^{-2}\mathrm{s}^{-1}$, while as the shared area shows the variation in the current densities based on k_0 range (see main text). The subscripts in NPs indicate the carbon chemical potential at which the NPs are synthesized.

Among the ten surfaces, (011) has the best HER activity followed by (001)-C, (100)-C, (110), (101), (010)-Mo, (021), (111)-Mo, (100)-Mo, and (001)-Mo. Note here that surfaces with exposed C atoms are close to the volcano peak with $\Delta G_{H^*} \approx 0$, while as the Mo-terminated polar surfaces which bind hydrogen more strongly are all at the tail of the volcano curve. This is in line with Sabatier principle[83]. The HER activities of NP_{-6} and NP_{-8} are comparable to that of (011)

because the NPs expose 62% and 83% of (011) termination. On the other hand, the NP_{-10} and NP_{-11}, have low exchange current densities because they expose smaller fraction of (011). In conclusion, the exchange current density for the NPs synthesized under $\mu_C = -8$ eV is about ~10^{-5} A/cm^2, which is similar to the high values reported experimentally (**Table 13**). Both thermal contribution and carbon chemical potential are essential for ΔG_{H^*} to approach its optimum value zero; however, these two factors have to work cooperatively especially for the range between μ_C=-8 and -11 eV at which the relative stability of surfaces are sensitive to temperature.

HER usually takes place in acidic solution. However, we assume that the hydrogen coverage, that is, the hydrogen adsorption is based on merely the factors of temperature and hydrogen partial pressure without considering water effects on the system. To avoid the complexity of thermodynamic environments, we provide the result with no thermodynamic factors. Here, both of ΔG_{H^*} and $\log(j_0)$ for β-Mo_2C NPs are within 7 % compare to the study with thermodynamic analysis. We conclude that our system is not sensitive with temperature and hydrogen partial pressure, and, possibly the other thermodynamic factors.

At HER measurement conditions, kinetic hindrances might be important as well as effects of the solvent. Previous studies suggest that kinetic effects are likely small as the hydrogen dissociation is barrierless for (001)-Mo, and has activation energies of 0.14, 0.34 and 0.20 eV for (100)-Mo, (011) and (021), respectively[41]. Further, previous DFT calculations showed that the effect of water changed the adsorption energy of Hydrogen on Pt surface by only less than 0.02 eV.[45] Because the adsorption of hydrogen on Mo_2C is stronger than that of the hydrogen on Pt, we expect that solvent effects will be even smaller. Nevertheless, more investigations are needed to delineate their effects more carefully following the previous study[84].

Table 13. Exchange current densities of β-Mo_2C NPs summarized from different experiments.

J_0 (A/cm^{-2})	**Electrolyte**	**Synthesis Method**
1.729 e-5 (Ref. 36)	0.1 M HClO4	solution route
2.683 e-6 / 1.037 e-5 (Ref. 44)	0.5M H_2SO_4 / 1M KOH	urea glass route
1.3 e-6 / 3.8 e-6 (Ref. 85)	1M H_2SO_4 / 1M KOH	commercial NPs
3.3 e-5 (Ref. 80)	0.5M H_2SO_4	solution route
7.94e-7 (Ref. 86)	0.5M H_2SO_4	carburization with CH4
7.38e-7 (Ref. 70)	1 M KOH	commercial
1.95e-6 / 3.43e-5 (Ref. 69)	0.5M H2SO4	Commercial/ solution route
4.0e-5 (Ref. 87)	0.05MH2SO4	mpg-C3N4 a
4.22e-6 (Ref. 47)	0.5M H_2SO_4	solution route
3.79e-6 (Ref. 81)	0.5M H_2SO_4	solution route
3.80e-6 (Ref. 82)	0.5M H_2SO_4	solution route
7.9e-7 (Ref. 88)	0.5M H_2SO_4	MoO4 H_2O

HER usually takes place in acidic solution. However, we assume that the hydrogen coverage, that is, the hydrogen adsorption is based on merely the factors of temperature and hydrogen partial pressure without considering water effects on the system. To avoid the complexity of thermodynamic environments, we provide the result with no thermodynamic factors. Here, both of ΔG_{H^*} and $\log(j_0)$ for β-Mo_2C NPs are within 7 % compare to the study with thermodynamic analysis (**Table 14**). We conclude that our system is not sensitive to temperature and hydrogen partial pressure, and, possibly the other thermodynamic factors.

Table 14. The log of exchange current density of NPs in vacuum and hydrogen gas environment.

β-Mo_2C NPs at 1000K	hydrogen gas environment (Log j)	Vacuum (Log j)
NP_{-6}	-4.91	-4.63
NP_{-7}	-4.83	-4.54
NP_{-8}	-4.79	-4.50
NP_{-9}	-4.77	-4.47
NP_{-10}	-8.09	-7.72
NP_{-11}	-8.30	-7.78

CONCLUSIONS

Methods to control the morphology of NPs are highly coveted in the field of catalysis. Here, we demonstrate that the synthesis of β-Mo_2C NPs by controlling the chemical potential from the range of μ_C=-6 and μ_C=-9 eV will yield β-Mo_2C NPs with large percentage of the catalytic (011) terminations. This provides a handle to tune the HER efficiency and we predict that optimum NPs for HER that expose 90% of the catalytic (011) can be synthesized with carbon chemical potential μ_C =-9 eV. In our study, we demonstrate the HER activity of β-Mo_2C NPs by considering only the percentage of each exposed surface termination. The focus on surface rather than edges between two surfaces is justified because synthesized NPs are over 5 nm in diameter[36,69,81,82,87], which makes the edges contribution to exchange currents negligible. Based on volcano relationship, we show that the exchange current densities of the optimum designed NPs are ~10^{-5} A/cm^2, which is only slightly smaller than that of Pt (111).

REFERENCE

1 Zhu, L., Li, L. & Fan, J. A modified process for overcoming the drawbacks of conventional steam methane reforming for hydrogen production: Thermodynamic investigation. *Chemical Engineering Research and Design* **104**, 792-806, doi:10.1016/j.cherd.2015.10.022 (2015).

2 Newson, E. Low-temperature catalytic partial oxidation of hydrocarbons (C1–C10) for hydrogen production. *International Journal of Hydrogen Energy* **28**, 1379-1386, doi:10.1016/s0360-3199(03)00005-3 (2003).

3 Wang, H. *et al.* Thermodynamic analysis of hydrogen production from glycerol autothermal reforming. *International Journal of Hydrogen Energy* **34**, 5683-5690, doi:10.1016/j.ijhydene.2009.05.118 (2009).

4 Deluga, G. A., Salge, J. R., Schmidt, L. D. & Verykios, X. E. Renewable hydrogen from ethanol by autothermal reforming. *Science* **303**, 993+ (2004).

5 Cormos, C.-C. Evaluation of iron based chemical looping for hydrogen and electricity co-production by gasification process with carbon capture and storage. *International Journal of Hydrogen Energy* **35**, 2278-2289, doi:10.1016/j.ijhydene.2010.01.033 (2010).

6 Kothari, R., Buddhi, D. & Sawhney, R. L. Comparison of environmental and economic aspects of various hydrogen production methods. *Renewable and Sustainable Energy Reviews* **12**, 553-563, doi:10.1016/j.rser.2006.07.012 (2008).

7 Carmo, M., Fritz, D. L., Mergel, J. & Stolten, D. A comprehensive review on PEM water electrolysis. *International Journal of Hydrogen Energy* **38**, 4901-4934, doi:10.1016/j.ijhydene.2013.01.151 (2013).

8 Parsons, R. The Rate of Electrolytic Hydrogen Evolution and the Heat of Adsorption of Hydrogen *Trans. Faraday Soc.* **54**, 1053-1063 (1957).

9 Kong, D., Cha, J. J., Wang, H., Lee, H. R. & Cui, Y. First-row transition metal dichalcogenide catalysts for hydrogen evolution reaction. *Energy & Environmental Science* **6**, 3553, doi:10.1039/c3ee42413h (2013).

10 Kibsgaard, J., Chen, Z., Reinecke, B. N. & Jaramillo, T. F. Engineering the surface structure of MoS2 to preferentially expose active edge sites for electrocatalysis. *Nat Mater* **11**, 963-969, doi:10.1038/nmat3439 (2012).

11 Laursen, A. B., Kegnæs, S., Dahl, S. & Chorkendorff, I. Molybdenum sulfides—efficient and viable materials for electro - and photoelectrocatalytic hydrogen evolution. *Energy & Environmental Science* **5**, 5577, doi:10.1039/c2ee02618j (2012).

12 Wang, T. *et al.* Size-Dependent Enhancement of Electrocatalytic Oxygen-Reduction and Hydrogen-Evolution Performance of MoS2 Particles. *Chemistry* **19**, 11939-11948, doi:10.1002/chem.201301406 (2013).

13 Ye, R. *et al.* High-Performance Hydrogen Evolution from MoS2(1-x) P x Solid Solution. *Adv Mater* **28**, 1427-1432, doi:10.1002/adma.201504866 (2016).

14 Voiry, D. *et al.* Conducting MoS(2) nanosheets as catalysts for hydrogen evolution reaction. *Nano Lett* **13**, 6222-6227, doi:10.1021/nl403661s (2013).

15 Vrubel, H., Merki, D. & Hu, X. Hydrogen evolution catalyzed by MoS3 and MoS2 particles. *Energy & Environmental Science* **5**, 6136, doi:10.1039/c2ee02835b (2012).

16 Lukowski, M. A. *et al.* Highly active hydrogen evolution catalysis from metallic WS2nanosheets. *Energy & Environmental Science* **7**, 2608, doi:10.1039/c4ee01329h (2014).

17 Schiros, T. *et al.* Connecting dopant bond type with electronic structure in N-doped graphene. *Nano Lett* **12**, 4025-4031, doi:10.1021/nl301409h (2012).

18 Xiao, P. *et al.* Molybdenum phosphide as an efficient electrocatalyst for the hydrogen evolution reaction. *Energy Environ. Sci.* **7**, 2624-2629, doi:10.1039/c4ee00957f (2014).

19 Chen, X. *et al.* Molybdenum phosphide: a new highly efficient catalyst for the electrochemical hydrogen evolution reaction. *Chem Commun (Camb)* **50**, 11683-11685, doi:10.1039/c4cc05936k (2014).

20 Jun, Y. S. *et al.* Three-dimensional macroscopic assemblies of low-dimensional carbon nitrides for enhanced hydrogen evolution. *Angew Chem Int Ed Engl* **52**, 11083-11087, doi:10.1002/anie.201304034 (2013).

21 Lau, V. W. *et al.* Low-molecular-weight carbon nitrides for solar hydrogen evolution. *J Am Chem Soc* **137**, 1064-1072, doi:10.1021/ja511802c (2015).

22 Meyer, S. *et al.* Transition metal carbides (WC, Mo2C, TaC, NbC) as potential electrocatalysts for the hydrogen evolution reaction (HER) at medium temperatures. *International Journal of Hydrogen Energy* **40**, 2905-2911, doi:10.1016/j.ijhydene.2014.12.076 (2015).

23 Esposito, D. V., Hunt, S. T., Kimmel, Y. C. & Chen, J. G. A new class of electrocatalysts for hydrogen production from water electrolysis: metal monolayers supported on low-cost transition metal carbides. *J Am Chem Soc* **134**, 3025-3033, doi:10.1021/ja208656v (2012).

24 Miyaoka, H., Ichikawa, T. & Kojima, Y. Thermochemical Energy Storage by Water-splitting Via Redox Reaction of Alkali Metals. *Energy Procedia* **49**, 927-934, doi:10.1016/j.egypro.2014.03.100 (2014).

25 Fujishima, A. & Honda, K. Electrochemical Photolysis of Water at a Semiconductor Electrode. *Nature* **238**, 37-38 (1971).

26 Chen, X. & Shangguan, W. Hydrogen production from water splitting on CdS-based photocatalysts using solar light. *Frontiers in Energy* **7**, 111-118, doi:10.1007/s11708-012-0228-4 (2013).

27 Ye, S., Wang, R., Wu, M.-Z. & Yuan, Y.-P. A review on g-C3N4 for photocatalytic water splitting and CO2 reduction. *Applied Surface Science* **358**, 15-27, doi:10.1016/j.apsusc.2015.08.173 (2015).

28 Markovic, N. M., Grgur, B. N. & Ross, P. N. Temperature-Dependent Hydrogen Electrochemistry on Platinum Low-Index Single-Crystal

Surfaces in Acid Solutions. *J. Phys. Chem. B* **101**, 8 (1997).

29 Skulason, E. *et al.* Density functional theory calculations for the hydrogen evolution reaction in an electrochemical double layer on the Pt(111) electrode. *Phys Chem Chem Phys* **9**, 3241-3250, doi:10.1039/b700099e (2007).

30 Chen, Y. *et al.* Facile Synthesis and Thermal Stability of Nanocrystalline Molybdenum Carbide. *Materials Sciences and Applications* **02**, 1313-1316, doi:10.4236/msa.2011.29178 (2011).

31 Wang, X.-H., Hao, H.-L., Zhang, M.-H., Li, W. & Tao, K.-Y. Synthesis and characterization of molybdenum carbides using propane as carbon source. *Journal of Solid State Chemistry* **179**, 538-543, doi:10.1016/j.jssc.2005.11.009 (2006).

32 Zhu, Q., Chen, Q., Yang, X. & Ke, D. A new method for the synthesis of molybdenum carbide. *Materials Letters* **61**, 5173-5174, doi:10.1016/j.matlet.2007.04.056 (2007).

33 Mo, T., Xu, J., Yang, Y. & Li, Y. Effect of carburization protocols on molybdenum carbide synthesis and study on its performance in CO hydrogenation. *Catalysis Today* **261**, 101-115, doi:10.1016/j.cattod.2015.07.014 (2016).

34 Roohi, P., Alizadeh, R. & Fatehifar, E. Thermodynamic study and methanothermal temperature-programmed reaction synthesis of molybdenum carbide. *International Journal of Minerals, Metallurgy, and Materials* **23**, 339-347, doi:10.1007/s12613-016-1243-y (2016).

35 Posada-Pérez, S., dos Santos Politi, J. R., Viñes, F. & Illas, F. Methane capture at room temperature: adsorption on cubic δ-MoC and orthorhombic β-Mo2C molybdenum carbide (001) surfaces. *RSC Adv.* **5**, 33737-33746, doi:10.1039/c4ra17225f (2015).

36 Wan, C., Regmi, Y. N. & Leonard, B. M. Multiple phases of molybdenum carbide as electrocatalysts for the hydrogen evolution reaction. *Angew Chem Int Ed Engl* **53**, 6407-6410, doi:10.1002/anie.201402998 (2014).

37 Hakan W. Hugosson, O. E., Lars Nordström, Ulf Jansson, Lars Fast, Anna Delin, John M. Wills, Borje Johansson. Theory of phase stabilities and bonding mechanisms in stoichiometric and substoichiometric molybdenum carbide. *J. Appl. Phys.* **86**, 3758 (1999).

38 Asara, G. G. *et al.* New Insights into the Structure of the C-Terminated β-Mo2C (001) Surface from First-Principles Calculations. *The Journal of Physical Chemistry C* **118**, 19224-19231, doi:10.1021/jp505847g (2014).

39 J. Haines, J. M. L., C. Chateau, J. E. Lowther. Experimental and theoretical investigation of Mo2C at high pressure. *Journal of Physics: Condensed Matter* **13**, 2447-2454 (2001).

40 Shi, X.-R. *et al.* Structure and stability of β-Mo2C bulk and surfaces: A density functional theory study. *Surface Science* **603**, 852-859, doi:10.1016/j.susc.2009.01.041 (2009).

41 Wang, T., Li, Y.-W., Wang, J., Beller, M. & Jiao, H. Dissociative Hydrogen Adsorption on the Hexagonal Mo2C Phase at High Coverage. *The Journal of Physical Chemistry C* **118**, 8079-8089, doi:10.1021/jp501471u (2014).

42 Wang, T., Wang, S., Li, Y.-W., Wang, J. & Jiao, H. Adsorption Equilibria of CO Coverage on β-Mo2C Surfaces. *The Journal of Physical Chemistry C* **116**, 6340-6348, doi:10.1021/jp300422g (2012).

43 Wang, T. *et al.* Stability of β-Mo2C Facets from ab Initio Atomistic Thermodynamics. *The Journal of Physical Chemistry C* **115**, 22360-22368, doi:10.1021/jp205950x (2011).

44 Ma, L., Ting, L. R. L., Molinari, V., Giordano, C. & Yeo, B. S. Efficient hydrogen evolution reaction catalyzed by molybdenum carbide and molybdenum nitride nanocatalysts synthesized via the urea glass route. *J. Mater. Chem. A* **3**, 8361-8368, doi:10.1039/c5ta00139k (2015).

45 Chen, W. F. *et al.* Highly active and durable nanostructured molybdenum carbide electrocatalysts for hydrogen production. *Energy & Environmental Science* **6**, 943, doi:10.1039/c2ee23891h (2013).

46 Sljukic, B. *et al.* Molybdenum Carbide Nanoparticles on Carbon Nanotubes and Carbon Xerogel: Low-Cost Cathodes for Hydrogen Production by Alkaline Water Electrolysis. *ChemSusChem* **9**, 1200-1208, doi:10.1002/cssc.201501651 (2016).

47 Pan, L. F. *et al.* Molybdenum carbide stabilized on graphene with high electrocatalytic activity for hydrogen evolution reaction. *Chem Commun (Camb)* **50**, 13135-13137, doi:10.1039/c4cc05698a (2014).

48 Li, J. S. *et al.* Coupled molybdenum carbide and reduced graphene oxide electrocatalysts for efficient hydrogen evolution. *Nat Commun* **7**, 11204, doi:10.1038/ncomms11204 (2016).

49 Zhang, K., Zhao, Y., Fu, D. & Chen, Y. Molybdenum carbide nanocrystal embedded N-doped carbon nanotubes as electrocatalysts for hydrogen generation. *J. Mater. Chem. A* **3**, 5783-5788, doi:10.1039/c4ta06706a (2015).

50 Ping Liu, J. A. R. Water-Gas-Shift Reaction on Molybdenum Carbide Surfaces: Essential Role of the Oxycarbide. *J. Phys. Chem.* **110**, 19418-19425 (2006).

51 Posada-Perez, S. *et al.* The bending machine: CO2 activation and hydrogenation on delta-MoC(001) and beta-Mo2C(001) surfaces. *Phys Chem Chem Phys* **16**, 14912-14921, doi:10.1039/c4cp01943a (2014).

52 Neyerlin, K. C., Gu, W., Jorne, J. & Gasteiger, H. A. Study of the Exchange Current Density for the Hydrogen Oxidation and Evolution Reactions. *Journal of The Electrochemical Society* **154**, B631, doi:10.1149/1.2733987 (2007).

53 Tsai, C., Abild-Pedersen, F. & Norskov, J. K. Tuning the MoS(2) edge-site activity for hydrogen evolution via support interactions. *Nano Lett* **14**, 1381-1387, doi:10.1021/nl404444k (2014).

54 Zhou, Z., Han, F., Guo, L. & Prezhdo, O. V. Understanding divergent behaviors in the photocatalytic hydrogen evolution reaction on CdS and ZnS: a DFT based study. *Phys Chem Chem Phys* **18**, 16862-16869, doi:10.1039/c6cp02599d (2016).

55 Qu, Y., Pan, H., Kwok, C. T. & Wang, Z. A first-principles study on the hydrogen evolution reaction of VS2 nanoribbons. *Phys Chem Chem Phys* **17**, 24820-24825, doi:10.1039/c5cp04118j (2015).

56 Zhang, H. *et al.* Active Sites Implanted Carbon Cages in Core-Shell Architecture: Highly Active and Durable Electrocatalyst for Hydrogen Evolution Reaction. *ACS Nano* **10**, 684-694, doi:10.1021/acsnano.5b05728 (2016).

57 Vasić Anićijević, D. D., Nikolić, V. M., Marčeta-Kaninski, M. P. & Pašti, I. A. Is platinum necessary for efficient hydrogen evolution? – DFT study of metal monolayers on tungsten carbide. *International Journal of Hydrogen Energy* **38**, 16071-16079, doi:10.1016/j.ijhydene.2013.09.079 (2013).

58 Reuter, K. & Scheffler, M. Composition, structure, and stability ofRuO2(110)as a function of oxygen pressure. *Physical Review B* **65**, doi:10.1103/PhysRevB.65.035406 (2001).

59 Chase, M. W. *et al.* JANAF Thermochemical Tables, 1982 Supplement. *Journal of Physical and Chemical Reference Data* **11**, 695, doi:10.1063/1.555666 (1982).

60 G. Kresse, J. F. Efficient iterative schemes for ab initio total-energy calculations using a plane-wave basis set. *Phys. Rew.* **54**, 11168 (1996).

61 John P. Perdew, K. B., Matthias Ernzerhof. Generalized Gradient Approximation Made Simple. *Physical Review Letters* **77**, 4 (1996).

62 Blochl, P. E. Projector augmented-wave method. *Phys Rev B* **50**, 17953-17979, doi:DOI 10.1103/PhysRevB.50.17953 (1994).

63 Kresse, G. & Joubert, D. From ultrasoft pseudopotentials to the projector augmented-wave method. *Phys Rev B* **59**, 1758-1775, doi:DOI 10.1103/PhysRevB.59.1758 (1999).

64 Tang, C. *et al.* Sulfur-Decorated Molybdenum Carbide Catalysts for Enhanced Hydrogen Evolution. *ACS Catalysis* **5**, 6956-6963, doi:10.1021/acscatal.5b01803 (2015).

65 Wan, C., Knight, N. A. & Leonard, B. M. Crystal structure and morphology control of molybdenum carbide nanomaterials synthesized from an amine-metal oxide composite. *Chem Commun (Camb)* **49**, 10409-10411, doi:10.1039/c3cc46551a (2013).

66 Sheng, W., Gasteiger, H. A. & Shao-Horn, Y. Hydrogen Oxidation and Evolution Reaction Kinetics on Platinum: Acid vs Alkaline Electrolytes. *Journal of The Electrochemical Society* **157**, B1529, doi:10.1149/1.3483106 (2010).

67 Rheinlander, P. J., Herranz, J., Durst, J. & Gasteiger, H. A. Kinetics of the Hydrogen Oxidation/Evolution Reaction on Polycrystalline Platinum in Alkaline Electrolyte Reaction Order with Respect to Hydrogen Pressure. *Journal of the Electrochemical Society* **161**, F1448-F1457, doi:10.1149/2.0501414jes (2014).

68 Patel, M. & Subrahmanyam, J. Synthesis of nanocrystalline molybdenum carbide (Mo2C) by solution route. *Materials Research Bulletin* **43**, 2036-2041, doi:10.1016/j.materresbull.2007.09.025 (2008).

69 Mu, Y. *et al.* Controllable synthesis of molybdenum carbide nanoparticles embedded in porous graphitized carbon matrixes as efficient electrocatalyst for hydrogen evolution reaction. *Electrochimica Acta* **215**, 357-365, doi:10.1016/j.electacta.2016.08.104 (2016).

70 Wu, Z.-Y. *et al.* Mo2C nanoparticles embedded within bacterial cellulose-derived 3D N-doped carbon nanofiber networks for efficient hydrogen evolution. *NPG Asia Materials* **8**, e288, doi:10.1038/am.2016.87 (2016).

71 Al-Saidi, W. A., Feng, H. & Fichthorn, K. A. Adsorption of polyvinylpyrrolidone on Ag surfaces: insight into a structure-directing agent. *Nano Lett* **12**, 997-1001, doi:10.1021/nl2041113 (2012).

72 Saidi WA, F. H., Fichthorn KA. Binding of Polyvinylpyrrolidone to Ag Surfaces: Insight into a Structure-Directing Agent from Dispersion-Corrected Density Functional Theory. *The Journal of Physical Chemistry C* **117**, 9 (2013).

73 Zhou Y, S. W., Fichthorn KA. Comparison of the binding of polyvinylpyrrolidone and polyethylene oxide to Ag surfaces: elements of a successful structure-directing agent. *The Journal of Physical Chemistry C* **117**, 5 (2013).

74 Zhou Y, S. W., Fichthorn KA. A Force Field for Describing the Polyvinylpyrrolidone-Mediated Solution-Phase Synthesis of Shape-Selective Ag Nanoparticles. *The Journal of Physical Chemistry C* **118**, 9 (2014).

75 Liu S-H, S. W., Zhou Y, Fichthorn KA. Synthesis of {111}-Faceted Au Nanocrystals Mediated by Polyvinylpyrrolidone: Insights from Density-Functional Theory and Molecular Dynamics. *The Journal of Physical Chemistry C* **119**, 9 (2015).

76 Ahmad Hanif, T. X., Andrew P. E. York, Jeremy Sloan, and Malcolm L. H. Green. Study on the Structure and Formation Mechanism of Molybdenum Carbide. *Chem. Mater.* **14**, 1009-1015 (2002).

77 Barmparis, G. D., Lodziana, Z., Lopez, N. & Remediakis, I. N. Nanoparticle shapes by using Wulff constructions and first-principles calculations. *Beilstein J Nanotechnol* **6**, 361-368, doi:10.3762/bjnano.6.35 (2015).

78 Richard I. Masel, R. I. M., R.I. Masel. *Principles of Adsorption and Reaction on Solid Surfaces*. 1 edn, 240 (Wiley Interscience, 1996).

79 Nørskov, J. K. *et al.* Trends in the Exchange Current for Hydrogen Evolution. *Journal of The Electrochemical Society* **152**, J23, doi:10.1149/1.1856988 (2005).

80 Tang, C., Sun, A., Xu, Y., Wu, Z. & Wang, D. High specific surface area Mo2C nanoparticles as an efficient electrocatalyst for hydrogen evolution. *Journal of Power Sources* **296**, 18-22, doi:10.1016/j.jpowsour.2015.07.016 (2015).

81 He, C. & Tao, J. Synthesis of nanostructured clean surface molybdenum carbides on graphene sheets as efficient and stable hydrogen evolution reaction catalysts. *Chem Commun (Camb)* **51**, 8323-8325, doi:10.1039/c5cc01240f (2015).

82 He, C. & Tao, J. Exploration of the electrochemical mechanism of ultrasmall multiple phases molybdenum carbides nanocrystals for hydrogen evolution reaction. *RSC Adv.* **6**, 9240-9246, doi:10.1039/c5ra25367e (2016).

83 Laursen, A. B. *et al.* Electrochemical Hydrogen Evolution: Sabatier's Principle and the Volcano Plot. *Journal of Chemical Education* **89**, 1595-1599, doi:10.1021/ed200818t (2012).

84 Saidi, W. A. Oxygen Reduction Electrocatalysis Using N-Doped Graphene Quantum-Dots. *The Journal of Physical Chemistry Letters* **4**, 4160-4165, doi:10.1021/jz402090d (2013).

85 Heron Vrubel, X. H. Molybdenum Boride and Carbide Catalyze Hydrogen Evolution inboth Acidic and Basic Solutions. *Angewandte Chemie* **51**, 12703-12706 (2012).

86 Kelly, T. G., Lee, K. X. & Chen, J. G. Pt-modified molybdenum carbide for the hydrogen evolution reaction: From model surfaces to powder electrocatalysts. *Journal of Power Sources* **271**, 76-81, doi:10.1016/j.jpowsour.2014.07.179 (2014).

87 Alhajri, N. S., Anjum, D. H. & Takanabe, K. Molybdenum carbide–carbon nanocomposites synthesized from a reactive template for electrochemical hydrogen evolution. *Journal of Materials Chemistry A* **2**, 10548, doi:10.1039/c4ta00577e (2014).

88 Ang, H. *et al.* Hydrophilic Nitrogen and Sulfur Co-doped Molybdenum Carbide Nanosheets for Electrochemical Hydrogen Evolution. *Small* **11**, 6278-6284, doi:10.1002/smll.201502106 (2015).